Geochemistry, Geophysics, Geosystems®

AGU ADVANCING EARTH AND SPACE SCIENCE

RESEARCH ARTICLE
10.1029/2022GC010648

A Revised Estimate of Early Pliocene Global Mean Sea Level Using Geodynamic Models of the Patagonian Slab Window

Andrew Hollyday[1], Jacqueline Austermann[1], Andrew Lloyd[1], Mark Hoggard[2], Fred Richards[3], and Alessio Rovere[4,5]

[1]Lamont-Doherty Earth Observatory, Department of Earth and Environmental Sciences, Columbia University, New York, NY, USA, [2]Research School of Earth Sciences, Australian National University, Canberra, ACT, Australia, [3]Department of Earth Science & Engineering, Imperial College London, London, UK, [4]Center for Marine Environmental Sciences, MARUM, University of Bremen (DE), Bremen, Germany, [5]DAIS Department for Environmental Sciences, Informatics and Statistics, Venice, Italy

Abstract Paleoshorelines serve as measures of ancient sea level and ice volume but are affected by solid Earth deformation including processes such as glacial isostatic adjustment (GIA) and mantle dynamic topography (DT). The early Pliocene Epoch is an important target for sea-level reconstructions as it contains information about the stability of ice sheets during a climate warmer than today. Along the southeastern passive margin of Argentina, three paleoshorelines date to early Pliocene times (4.8–5.5 Ma), and their variable present-day elevations (36–180 m) reflect a unique topographic deformation signature. We use a mantle convection model to back-advect present-day buoyancy variations, including those that correspond to the Patagonian slab window. Varying the viscosity and initial tomography-derived mantle buoyancy structures allows us to compute a suite of predictions of DT change that, when compared to GIA-corrected shoreline elevations, makes it possible to identify both the most likely convection parameters and the most likely DT change. Our simulations illuminate an interplay of upwelling asthenosphere through the Patagonian slab window and coincident downwelling of the subducted Nazca slab in the mantle transition zone. This flow leads to differential upwarping of the southern Patagonian foreland since early Pliocene times, in line with the observations. Using our most likely DT change leads to an estimate of global mean sea level of 17.5 ± 6.4 m (1σ) in the early Pliocene Epoch. This confirms that sea level was significantly higher than present and can be used to calibrate ice sheet models.

Plain Language Summary Understanding the height of global mean sea level (GMSL) during the early Pliocene Epoch, when Earth's climate was warmer than today, will help to improve predictive models of current sea-level rise. In eastern Patagonia, shorelines that formed during this time period have been uplifted due to convective flow in the mantle beneath southern South America. We model both mantle flow and the effects of ice sheet loading changes, which also cause Earth's topography to evolve through time, to correct the present-day elevations of these shorelines. After subtracting out the effects of solid Earth deformation, we calculate a GMSL of 17.5 ± 6.4 m (1σ) in the early Pliocene Epoch.

Key Points:

- Mantle flow through the Patagonian slab window, coupled with slab ponding in the mantle transition zone, has uplifted eastern Patagonia since 5 Ma
- Accounting for the effects of solid Earth deformation through time, global mean sea level (GMSL) was 17.5 ± 6.4 m (1σ) in the early Pliocene Epoch
- Antarctic ice is estimated to have been smaller in the Pliocene by 9.5 ± 6.9 m of GMSL equivalent

Supporting Information:

Supporting Information may be found in the online version of this article.

Correspondence to:

A. Hollyday,
andrewh@ldeo.columbia.edu

Citation:

Hollyday, A., Austermann, J., Lloyd, A., Hoggard, M., Richards, F., & Rovere, A. (2023). A revised estimate of early Pliocene global mean sea level using geodynamic models of the Patagonian slab window. *Geochemistry, Geophysics, Geosystems*, *24*, e2022GC010648. https://doi.org/10.1029/2022GC010648

Received 3 AUG 2022
Accepted 19 DEC 2022

Author Contributions:

Conceptualization: Andrew Hollyday, Jacqueline Austermann
Data curation: Andrew Hollyday, Jacqueline Austermann, Alessio Rovere
Formal analysis: Andrew Hollyday, Jacqueline Austermann
Funding acquisition: Jacqueline Austermann
Investigation: Andrew Hollyday, Jacqueline Austermann, Andrew Lloyd, Mark Hoggard, Fred Richards

1. Introduction

As anthropogenic warming continues to melt continental ice and deliver it to the global oceans, mitigation plans will require more confident projections of sea-level rise. The capability of coupled ice-Earth-sea-level models to predict the amplitude and timing of sea-level rise during this century relies on uncertain calibrations of ice sheet sensitivity to variable amounts of warming in Earth's past (DeConto & Pollard, 2016; DeConto et al., 2021; Fischer et al., 2018). While the mid-Pliocene Epoch has already been used as a calibration target that significantly affects projections of future sea-level change (DeConto & Pollard, 2016; DeConto et al., 2021), the early Pliocene Epoch (5.3–3.6 Ma) has so far received less attention. This time consisted of interglacial global mean temperatures around 4°C higher than today and CO_2 concentrations above 400 ppm (Burke et al., 2018; Collins et al., 2013; Fedorov et al., 2013; Haywood et al., 2013; Pagani et al., 2010). Given rising temperature predictions for Earth's future, we believe that this time period serves as an increasingly important calibration target for ice sheet models (Burke et al., 2018).

The Pliocene sea-level calibrations used in the projections of DeConto et al. (2021) and DeConto and Pollard (2016) stem from a range of methodologies. While δ^{18}O-Mg/Ca-based inferences (e.g., Miller et al., 2012) provide some

Methodology: Andrew Hollyday, Jacqueline Austermann, Andrew Lloyd, Mark Hoggard, Fred Richards
Project Administration: Jacqueline Austermann
Resources: Andrew Hollyday, Jacqueline Austermann, Andrew Lloyd, Mark Hoggard, Fred Richards
Software: Andrew Hollyday, Jacqueline Austermann, Mark Hoggard, Fred Richards
Supervision: Jacqueline Austermann
Validation: Andrew Hollyday, Jacqueline Austermann
Visualization: Andrew Hollyday, Jacqueline Austermann
Writing – original draft: Andrew Hollyday, Jacqueline Austermann
Writing – review & editing: Andrew Hollyday, Jacqueline Austermann, Andrew Lloyd, Mark Hoggard, Fred Richards, Alessio Rovere

advantages, effects such as carbonate diagenesis and unconstrained sea water chemistry and salinity have led to high levels of uncertainty in global mean sea level (GMSL) estimates based on these proxies (Raymo et al., 2018; Rohling et al., 2014; Waelbroeck et al., 2002). Alternatively, mapping of paleoshorelines provides a direct measure of past relative sea level (RSL; Rovere et al., 2014). Nevertheless, due to processes such as tectonic deformation, local sediment loading, glacial isostatic adjustment (GIA), and mantle dynamic topography (DT), RSL records must be corrected for topographic changes in elevation since their deposition that cause local sea level to diverge from the global mean. To date, understanding and modeling these processes poses the biggest difficulty in reliably inferring GMSL during the Pliocene Epoch. In this work, we leverage variable uplift of Pliocene shorelines in Patagonia to constrain mantle flow, correct their elevations for deformation due to DT, and use the results to infer GMSL.

GIA describes the viscoelastic response of the solid Earth, its gravity field, and rotation axis to changes in ice and ocean loading. Raymo et al. (2011) examined its influence on Pliocene shorelines and found that GIA can cause changes in the far field of ice sheets of up to ∼10 m. This contribution emphasized the need to correct for GIA when inferring past GMSL from Pliocene shorelines. In addition to GIA, convection in Earth's interior driven by lateral density variations causes vertical deflections of Earth's surface and the geoid through time in what is termed DT (Hoggard et al., 2021). DT changes have been shown to significantly deform paleoshorelines. For example, Rowley et al. (2013) predicted changes in DT on the order of ∼50 m spanning the last 3 Myr and found that they correlate with variations in the elevation of the Orangeburg Scarp located along the U.S. East Coast. While the importance of correcting paleoshorelines for DT change is known (Austermann et al., 2017; Moucha & Ruetenik, 2017; Moucha et al., 2008; Rowley et al., 2013), reliable corrections are inhibited by under-resolved mantle structure as well as uncertainties in plate motion reconstructions and conversions from seismic wave speeds to mantle rheology, densities, temperatures, and viscosities.

Paleoshorelines that date to the early Pliocene Epoch are sparse (Dumitru et al., 2019; Hearty et al., 2020; Rovere et al., 2020), and given the challenges in modeling their geodynamic deformation, it is difficult to use them to obtain reliable GMSL estimates for this time period. The most confident early Pliocene estimate to date comes from Mallorca, Spain, where a GMSL of 25.1 m (median; 10.6–28.3 m, 16th to 84th percentile uncertainty bounds) at 4.39 ± 0.39 Ma (2σ) Ma was inferred from phreatic overgrowth on speleothems (Dumitru et al., 2019). Using an RSL record from South Africa mapped and dated by Hearty et al. (2020), Rovere et al. (2020) corrected for GIA and used the long-wavelength global convection models from Müller et al. (2018) to correct for DT change and estimate an early Pliocene GMSL of 23.4 ± 35.8 m (mean, 1σ). In Camarones, Argentina, Rovere et al. (2020) estimated GMSL of 28.4 ± 11.7 m (mean, 1σ) on the basis of a transgressive conglomerate unit containing bivalve and gastropod fauna dated to 4.96 ± 0.27 Ma (2σ), corrected for GIA using 1-D Earth models and DT change using models from Flament et al. (2015). In both the estimates from Argentina and South Africa, the DT correction introduced significant uncertainty into their GMSL inference as the convection model uncertainties were characterized by a wide range of model parameter choices. Higher confidence predictions can be achieved by comparing model results with additional geodynamic observations from regions of interest.

In this study, we revisit the Camarones site in Argentina (Rovere et al., 2020) as well as two sites to the south (within 600 km) that also exhibit early Pliocene shoreline deposits (del Río et al., 2013; Figure 1; Table 1). The three Patagonian deposits consist of fossiliferous, coarse-grained sandstone and gravel beds containing fragmented species of *Chlamys actinodes* (southern two localities; Cañadón Darwin and the Terrace of the Cerro Laciar) and cemented fine conglomerates with species from the Ostedidae family (northern locality; Camarones). These faunal assemblages have been sampled and analyzed, and their $^{87}Sr/^{86}Sr$ (Strontium Isotope Stratigraphy, SIS) ages fall in the interval from 5.33 to 4.69 Ma (2σ; del Río et al., 2013; Rovere et al., 2020), slightly predating the earliest Pliocene sea-level estimates from Mallorca and South Africa (Dumitru et al., 2019; Hearty et al., 2020). They occur at mean elevations of 70 ± 5, 177.5 ± 7.5, and 36.2 ± 2.7 m above sea level (south to north), along a near-longitudinal profile on the tectonically inactive passive margin of southern Argentina (Figure 1). The elevation uncertainties stem from instrumental and mapping error, as well as estimates for the water depth at which each species can grow (see del Río et al., 2013; Rovere et al., 2020). Noting the comparatively long-wavelength spatial patterns expected for GIA (Raymo et al., 2011), we hypothesize these sites, which show a clear short-wavelength (<600 km) topographic signature, have been deformed by convective mantle flow.

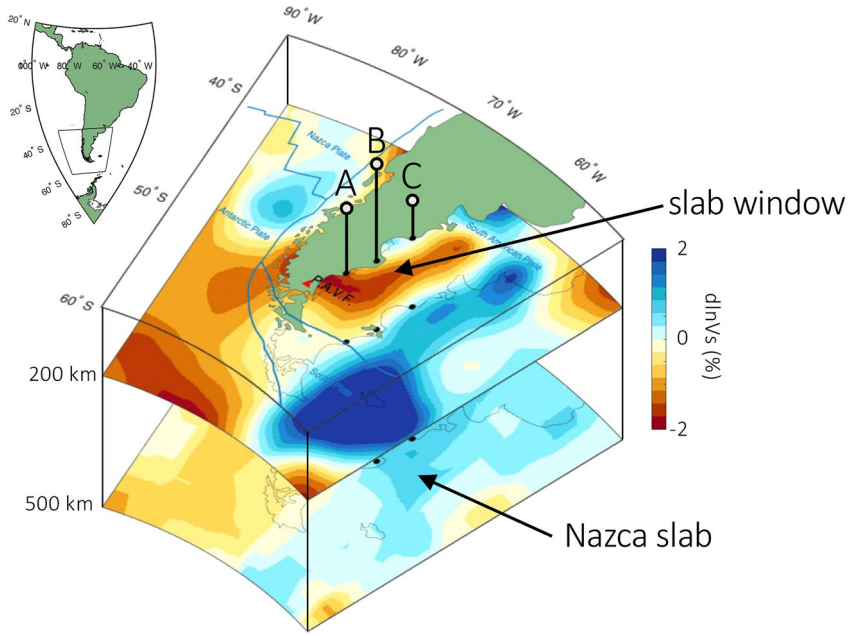

Figure 1. Schematic diagram of the Patagonian slab window. Sites A, B, and C correspond to uplifted sea level indicators that date to the early Pliocene Epoch. The upper mantle structure is imaged by the SL2013sv tomography model (Schaeffer & Lebedev, 2013), with slow seismic wave speeds at shallow depths (200 km). Transition zone structure (500 km) from the TX2011 tomography model (Grand, 2002) shows faster velocities that reflect the previously subducted Nazca slab. Sites A (Cañadón Darwin), B (Terrace of the Cerro Laciar), and C (Camarones) occur at mean elevations of 70 ± 5, 177.5 ± 7.5, and 36.2 ± 2.7 m above sea level, respectively.

We present mantle convection models constrained by inferences of mantle density structure obtained from global seismic tomography, combined with GIA models, to better understand how these three early Pliocene sea-level deposits were subsequently deformed. We use their differential elevation to investigate slab window subduction behavior and constrain Earth structure. We then combine results from DT and GIA modeling to correct their elevations for post-depositional effects and produce an inference of GMSL from the early Pliocene Epoch.

Table 1
Locations, Measured Elevations, Ages, and Geodynamic Corrections for the Three Paleoshorelines in Eastern Patagonia

	Site A (southernmost; del Río et al., 2013)	Site B (middle; del Río et al., 2013)	Site C (northernmost; Rovere et al., 2020)
	Cañadón Darwin	Terrace of the Cerro Laciar	Camarones
Latitude (°)	−49.628	−47.629	−44.790
Longitude (°)	−67.715	−66.392	−65.728
Elevation (m; 1σ)	70.0 ± 5.0	177.5 ± 7.5	36.2 ± 2.7
Age (Ma; 2σ)	5.15 ± 0.18	5.10 ± 0.21	4.96 ± 0.27
GIA correction (m; 1σ)	−10.4 ± 2.8	−10.5 ± 2.7	−11.4 ± 2.8
DT correction (m)	66.2	154.7	32.4

2. Tectonic Setting

The present-day tectonic configuration of Patagonia has evolved from a complex history of oceanic ridge convergence beneath the South American plate. By ∼20 Ma, subduction of the Nazca-Phoenix Ridge had generated a small slab window beneath the southern tip of Patagonia (∼66°S; Breitsprecher & Thorkelson, 2009). This early gap in the subducting slab expanded when the Nazca-Antarctic-Phoenix triple junction subducted beneath Patagonia at ∼18 Ma. This event led to southward migration of the subducting Phoenix-Antarctic Ridge. Simultaneously, the Nazca-Antarctic-South American triple junction migrated ∼1,000 km northward to ∼46.5°S until ∼4 Ma, where it has since remained stable (Breitsprecher & Thorkelson, 2009). Models suggest the Antarctic slab began subducting beneath Patagonia between these two triple junctions, but its upper surface has likely reached only ∼45 km depth due to the slow rate of convergence (Breitsprecher & Thorkelson, 2009). Finally, by ∼3.3 Ma, the Phoenix plate was captured by the Antarctic plate, which terminated the slow southward growth of the Patagonian slab window (Eagles, 2004; Livermore et al., 2000).

Opening of the slab window has led to regional mafic volcanism. Anhydrous Plio-Quaternary lavas with Ocean Island Basalt affinities likely sourced from beneath the slab have subsequently erupted across southern Patagonia,

approximately delineating the extent of the slab window (Gorring et al., 2003), with other, spatially anomalous eruptions linked to possible slab tearing (e.g., Guivel et al., 2006). Early stages of opening of the slab window are coincident with paleo heat flow-based estimates of lithospheric thinning and uplift of the Patagonian foreland (Ávila & Dávila, 2018, 2020; Rodriguez & Littke, 2001; Sachse et al., 2016); however, evidence is lacking for significant lithospheric thickness changes once the slab window reached a steady-state configuration at ∼4 Ma.

The 3-D geometry of the present-day subsurface slab window has been revealed by seismic tomography (Figure 1; Schaeffer & Lebedev, 2013). This structure, which consists of hot upwelling asthenosphere through the Patagonian slab window and coincident downwelling of the underlying remnant Nazca slab, is a probable setting for changes in DT through time that may be responsible for differential upwarping of the three observed early Pliocene paleoshorelines. While previous work (Ávila & Dávila, 2018, 2020; Dávila & Lithgow-Bertelloni, 2013; Dávila et al., 2019; Flament et al., 2015; Guillaume et al., 2009) has shed light on possible convection dynamics and deformation histories of the Patagonian foreland, we present a new generation of models that is directly constrained by seismically imaged present-day mantle structure.

3. Methods

With the goal of computing an early Pliocene GMSL, we reassess the deformational history of published sea-level deposits by (a) correcting the observed elevations of the shorelines for GIA (Section 3.1), (b) modeling a suite of mantle convection simulations that reproduce the dynamic behavior of the Patagonian slab window and short-wavelength DT patterns (Section 3.2), and (c) leveraging the different elevations of the shorelines, residual topography observations from the surrounding oceanic basins, and the early Pliocene sea-level observation from Mallorca to perform data-model comparison and constrain otherwise highly uncertain solutions of DT change (Section 3.3).

3.1. GIA Correction

To determine the contribution of GIA to deformation of the shorelines, we solve the gravitationally self-consistent sea-level equation for a depth dependent Maxwell viscoelastic Earth structure (Kendall et al., 2005). Our approach accounts for shoreline migration and the feedback of load changes into Earth's rotation axis. Following the approach described in Raymo et al. (2011) and Dumitru et al. (2019), we deconstruct the GIA signal into two parts: (a) the ongoing response to the last glacial cycle and (b) the response to ice sheet variability during the early Pliocene Epoch. We use a spherically symmetric elastic and density structure from the seismic reference model PREM (Dziewonski & Anderson, 1981). For the depth dependent viscosity structure, we combine two lithospheric thicknesses (71 and 96 km) with two upper mantle viscosities (3×10^{20} Pa s, 5×10^{20} Pa s) and six lower mantle viscosities (3×10^{21} Pa s, 5×10^{21} Pa s, 7×10^{21} Pa s, 1×10^{22} Pa s, 2×10^{22} Pa s), generating a total of 24 different radial Earth structures. The transition from upper to lower mantle is defined at 670 km depth. While radial viscosity profiles neglect known lateral variations revealed by seismic tomography (e.g., Ritsema et al., 2011; Russo et al., 2022), employing a range of estimates of mantle viscosity allows us to estimate the uncertainty introduced by this assumed 1-D structure.

For the first correction, we use an extension of the ICE-6G_C ice history which prescribes global ice extents from 122 ka to present-day (Peltier & Fairbanks, 2006; Peltier et al., 2015). We then allow our models to evolve past the present day until they reach steady-state isostasy, which enables us to estimate how much present-day shorelines are affected by the last glacial cycle. For the second correction, we account for GIA associated with excess melt during the Pliocene Epoch when ice sheets were smaller than today. With the same suite of radial Earth structures used for the first correction, we pair an ice history that varies Antarctic and—to a much smaller degree—Greenland ice volume following the LR04 benthic isotope stack (Lisiecki & Raymo, 2005). We use an ice reconstruction for Antarctica that is based on Pollard et al. (2015), who modeled the Antarctic ice sheet during the mid-Pliocene Epoch. This reconstruction, which consists of 41 m of sea level equivalent ice, represents an intermediate ice distribution characterized by major deglaciation of the West Antarctic Ice sheet (WAIS) and notable retreat from Wilkes Basin, Aurora Basin, and the Recovery Ice Stream (Cook et al., 2013; Naish et al., 2009; Pollard et al., 2015; Scherer et al., 2016). For the ice distribution in Greenland, we assume 50 cm of sea level equivalent ice stored along the eastern coast since this high terrain was likely the first to glaciate (Bierman et al., 2016). We then scale the ice height for this model uniformly up and down following the LR04

benthic isotope stack (Lisiecki & Raymo, 2005), which is scaled to GMSL using a conversion factor of 0.033 ‰ m^{-1}. This conversion was chosen to yield a GMSL during the early Pliocene Epoch that is consistent with our final result. That is, we iterate through potential conversion factors, correcting the paleoshorelines for GIA and DT (discussed in Section 3.2) until we obtain an early Pliocene GMSL within 0.5 m of the final inference. Since the exact interglacial that the early Pliocene shorelines formed during is unknown (due to geochronologic uncertainties), we take the GIA correction at seven possible interglacials that are consistent with the age uncertainties of the three shorelines (5.235, 5.135, 5.090, 5.020, 4.925, 4.874, and 4.825 Ma). Our ice reconstruction, used in our GIA models, yields early Pliocene GMSL ranging from 13.8 to 21.3 m during the seven interglacials. We note that GMSL is calculated as ice equivalent sea level assuming a fixed ocean area (see Dumitru et al., 2019). Finally, we combine the two GIA components, with respective radial Earth structures, to generate 168 different predictions (24 Earth structures × 7 interglacial ages) of deformation due to GIA. The GIA correction is treated as an ensemble of these predictions due to the small variations that result from the parameterizations detailed above.

3.2. Mantle Convection Simulations

We perform a suite of mantle convection simulations to discern the effects of changes in DT on the deformational history of the three early Pliocene paleoshorelines. To model convection we use the finite element convection code ASPECT, which solves the governing equations for mantle convection: conservation of mass, energy, and momentum employing state-of-the-art numerical methods (Bangerth, Dannberg, Gassmoeller, Heister, Myhill, & Naliboff, 2020; Heister et al., 2017; Kronbichler et al., 2012). We use ASPECT 2.2.0 to run global incompressible back-advection simulations for the mantle, which reverse flow through time, with free-slip boundary velocity conditions and thermal boundary conditions consistent with surface and core-mantle-boundary (CMB) temperatures (0°C and 3027°C, respectively). We note that our CMB thermal boundary condition is toward the lower end of previously inferred temperatures (Lay et al., 2008). We assign representative values for reference temperature (1,333°C), reference density (3,300 kg m^{-3}), and specific heat (1,250 J K^{-1} kg^{-1}). Thermal diffusivity is set to zero since diffusion is not a time-reversible process and would be minimal over a 5 Myr timespan. Radially varying gravity and thermal expansivity profiles are adopted from Glišović and Forte (2015). We pair three different viscosity models with six different temperature structures of the mantle resulting in a total of 18 time-dependent simulations.

The initial temperature structures of our mantle convection models are derived from seismic tomography. We use several tomographic models of shear wave speed and employ a different conversion from wave speed to temperature for the upper mantle (0–410 km) than the transition zone and lower mantle (410 km—CMB) since our upper mantle conversion method is only applicable to an olivine-dominated composition. All temperature models include a section of linearly merged temperatures between 300 and 400 km to prevent discontinuous jumps in the converted temperature models. The full conversion scheme from seismic velocities to temperatures in the upper mantle, transition zone, and lower mantle is illustrated in Supplementary Figure 1.

Upper mantle temperature is derived from two higher resolution velocity models: GLAD-M25 and SL2013sv (Lei et al., 2020; Schaeffer & Lebedev, 2013). SL2013sv was generated using only shorter period surface wave data, while GLAD-M25 also used body wave data. We convert to temperatures using an experimentally derived parameterization describing the anelastic properties of the mantle analog material, borneol, calibrated with geophysical observations (Richards et al., 2020; Yamauchi & Takei, 2016). Calibration targets are oceanic lithospheric temperatures, the radial attenuation structure of the upper mantle (Dalton et al., 2009), and the bulk upper mantle viscosity. We further require the average computed temperatures at each depth to be consistent with a 1,333°C reference temperature (Richards et al., 2020). The calibrated parameterization, which is based on tomography model-specific inversions of the seven free parameters of the Yamauchi and Takei (2016) formulation (parameters reported in Table S1 of Supporting Information S1), describes the full temperature domain of the velocity-to-temperature relationship including the high temperature segment, where using a purely anharmonic relation would lead to over-prediction of temperatures owing to the significant effects of anelastic deformation in the upper mantle (Richards et al., 2020). Within the continental lithosphere, temperatures converted from seismic velocities are highly uncertain due to compositional differences between the sublithospheric mantle and the continental lithosphere. Following Jordan (1978), we assume that continents are neutrally buoyant and therefore set, at each depth, the temperature within the continental lithosphere equal to the mean temperature outside of continents (as in Richards et al., 2020). We acknowledge, however, that recent work has suggested

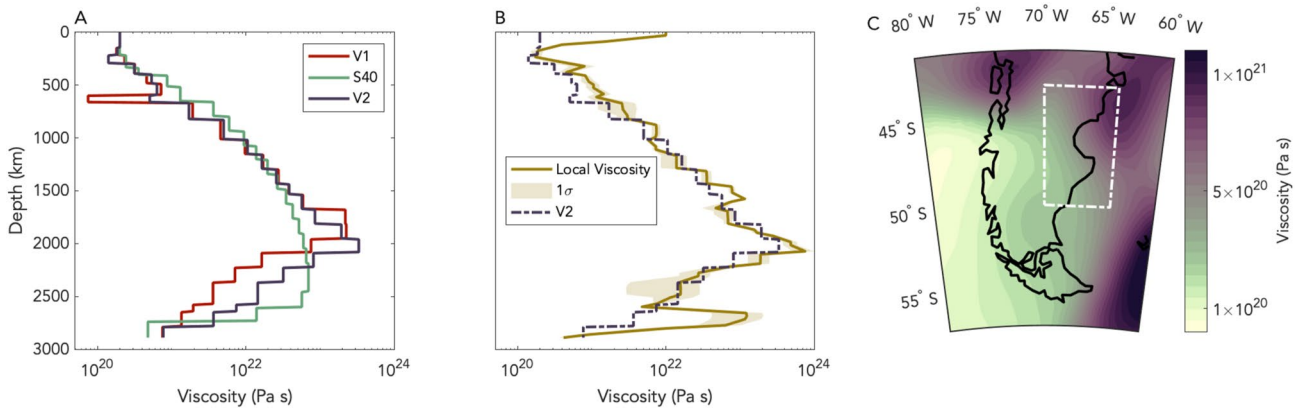

Figure 2. (a) Radial viscosity profiles used in the mantle convection suite. These profiles are scaled laterally according to the different 3D tomography-derived mantle temperature models. (b) Local depth-averaged viscosity structure from within the white rectangle (shown on the map in (c)) from a best-fitting convection model that uses the laterally scaled V2 radial profile. Associated 1σ viscosity variations are shown in the shaded tan envelope. (c) A map of lateral viscosity variations at 300 km depth. Model shown in (b and c) is from SL2013sv upper mantle and TX2011 transition zone and lower mantle structure (Grand, 2002; Schaeffer & Lebedev, 2013).

that continental lithosphere may be denser than indicated by the isopycnic assumption (Y. Wang et al., 2022). Changes in temperature and thickness of the oceanic lithosphere leads to a significant topographic signal due to isostasy. This signal and its resulting change through time is sometimes but not always included in the definition and modeling of DT (Forte et al., 1993; Hoggard et al., 2021). Here we treat the oceanic lithosphere as neutrally buoyant (i.e., set the temperature to follow the same depth profile as within the continents) since changes in DT driven by ocean lithosphere cooling are expected to be minimal in the Argentine Abyssal Plain, which evolved to full seafloor spreading in mid-Cretaceous times. We perform an independent assessment of the tomography-based temperature models by comparing them to the equilibration pressures and temperatures of mantle xenoliths (Table S2 in Supporting Information S1) erupted from the Pali-Aike Volcanic Field in southern Patagonia (J. Wang et al., 2008). These thermobarometry calculations use measured major element compositions from olivine, orthopyroxene, clinopyroxene, and garnet that are hosted in high-temperature (>900°C) peridotites, garnet-spinel harzburgites, and garnet lherzolites dated to Plio-Quaternary times (Bhanot et al., 2020; Nickel & Green, 1985; Taylor, 1998; J. Wang et al., 2008).

Structure in the lower mantle and transition zone (below 400 km) is obtained from three lower resolution, global tomography models: TX2011, S362ANI + M, and S40RTS (Grand, 2002; Moulik & Ekström, 2014; Ritsema et al., 2011). We convert relative seismic wave velocities to relative densities using a simple linear scaling with a depth-varying conversion factor from Steinberger (2016). We use a linearly interpolated depth-varying thermal expansion profile based on Glišović and Forte (2015) to convert density perturbations to relative temperatures. We assign reference values that are consistent with the convection parameters detailed above.

Viscosity is assumed to vary radially and laterally. We use three radial viscosity profiles that come from inversions of GIA and convection observables (Figure 2a; Forte et al., 2010; Mitrovica & Forte, 2004; Steinberger, 2016). To enforce a more rigid lithosphere while limiting sharp viscosity contrasts that otherwise cause shallow small-scale convection and model artifacts in our DT predictions, we first set all radial profiles to 2×10^{20} Pa s above 150 km, then assign a constant viscosity of 1×10^{22} Pa s above the lithosphere-asthenosphere boundary (LAB), which is defined as the 1,200°C isotherm specific to each temperature model (described below). We lastly assign a viscosity of 5×10^{21} Pa s between the LAB and 120% of its depth to smooth vertical viscosity variations. Lateral variability is introduced through an Arrhenius relationship:

$$\eta(z,T) = \eta_r(z) e^{\frac{-A(T-T_r)}{T_r}}, \quad (1)$$

where $\eta(z, T)$ is the mantle viscosity that varies with both depth, z, and the laterally variable temperature, T, $\eta_r(z)$ is the radial reference viscosity, T_r is the reference incompressible temperature set to 1,333°C, and A is a thermal viscosity exponent set to 0.01 (Figures 2b and 2c; see Bangerth, Dannberg, Gassmoeller, Heister, Myhill, & Naliboff, 2020, p. 163 for details). Note that viscosity remains constant at depths ≤120% of the LAB and is not scaled laterally by temperature as is the case through the remainder of the mantle.

DT is calculated from radial stresses at the surface and the density contrast between the crust and the overlying material (Zhong et al., 1993). We take into account that the overburden changes from air to water along the shorelines following the method outlined in Austermann and Mitrovica (2015), using a 90 km-thick lithosphere. Estimates based on surface heat flow report lithospheric thicknesses beneath Patagonia of ~40–70 km (Ávila & Dávila, 2018), while global estimates of the thermal LAB from surface-wave seismology find it deeper ~110 km (Priestley et al., 2018). In addition, both our seismic tomography-derived temperature estimates and calculations from mantle xenoliths suggest the regional LAB is around 90 km (Figure 5). Given this lack of consensus, our choice of 90 km-thick lithosphere represents an intermediate selection. We further test the sensitivity of lithospheric thickness to the inferred GMSL, which is discussed in Section 5.2. Convection-caused perturbations to the geoid are also accounted for and included in the final calculation of change in DT since we are interested in sea-level changes rather than just solid Earth deformation. Our convection simulations back-advect the present-day mantle structure for 5 Myr and calculate DT and geoid anomalies at each timestep (geoid changes are included in our use of "DT changes" for the remainder of the manuscript). Our calculations are incompressible through the Boussinesq approximation, which is not directly compatible with some assumptions made in the model; however, we expect these to be second order effects in comparison to accurately constraining the mantle's density structure. We do not include phase changes, thermal boundary layers, internal radiogenic heat production, or deflection of internal boundaries within the simulations; however, the initial temperature structures we prescribe implicitly include some of these important dynamics. While we do not model brittle deformation in the crust within our simulations, the absence of mapped neotectonic structures (e.g., faulting) in this region indicates minimal crustal deformation has occurred since the Pliocene Epoch (Perucca et al., 2016).

To calculate the change in DT through time, we must take into account how the motion of tectonic plates has displaced DT fields over time (Czarnota et al., 2013; Lithgow-Bertelloni & Gurnis, 1997; Sandiford, 2007). This postprocessing correction accounts for the total rotation of the lithosphere relative to the mantle, as well as the motion of tectonic plates relative to one another. First we rotate global plates ($n = 56$) relative to each other in a no-net-rotation reference frame from Argus et al. (2011) and then apply a total lithospheric rotation of 0.25° Ma^{-1} right-handed about 57.1°S, 68.6°E from Zheng et al. (2014). We explore the total rotation uncertainty by also including results rotated by 1σ (0.195 and 0.305° Ma^{-1}) and 2σ (0.14 and 0.36° Ma^{-1}) of their stated uncertainty. We note that a total lithospheric rotation is applied in this postprocessing procedure since we impose no-net-rotation in the suite of reverse-advection simulations.

3.3. Data-Model Comparison

We first correct the observed elevations, E, of the three early Pliocene shorelines for GIA by subtracting the mean GIA correction, $\overline{\mathrm{GIA}_i}$, (averaged over different Earth structures and different interglacials) from the mean observed elevation of paleo sea level at each location, i. This yields the GIA-corrected elevation, $\overline{\mathrm{GE}_i}$:

$$\overline{\mathrm{GE}_i} = \overline{E_i} - \overline{\mathrm{GIA}_i} \tag{2}$$

and associated uncertainty, σ_{GE_i}:

$$\sigma_{\mathrm{GE}_i} = \sqrt{\sigma_{E_i}^2 + \sigma_{\mathrm{GIA}_i}^2}, \tag{3}$$

where σ_{E_i} is the uncertainty in elevation measurements and indicative range or habitable water depth for the observed species (see del Río et al., 2013; Rovere et al., 2020) and σ_{GIA_i} is the uncertainty in the GIA correction due to variable Earth structure and ice loading. Rovere et al. (2020) incorporated an estimate for indicative range into their reported RSL elevation. While del Río et al. (2013) does not explicitly report indicative range in their elevation uncertainty, the reported uncertainty of 15 m (2σ) reflects a conservative estimate.

Next, we compare the GIA-corrected elevations to our DT predictions. To do so we subtract the DT prediction, $\mathrm{DT}_{i,m}$, where m specifies the DT model, from the GIA-corrected elevation ($\overline{\mathrm{GE}_i}$) at each site to obtain a GMSL estimate for this site:

$$\mathrm{GMSL}_{i,m} = \overline{\mathrm{GE}_i} - \mathrm{DT}_{i,m} \tag{4}$$

We then calculate a GMSL as the weighted mean between the three sites, where weights are the squared inverse of the uncertainty in GIA-corrected elevation at each site:

$$w_i = {}^{1}/_{\sigma^2_{\mathrm{GE}_i}} \tag{5}$$

$$\mathrm{GMSL}_m = \frac{\sum_{i=1}^{N}(w_i \cdot \mathrm{GMSL}_{i,m})}{\sum_{i=1}^{N} w_i}, \tag{6}$$

where N is the number of shorelines ($N = 3$). This is performed for each DT prediction, m, which in total consists of 90 predictions (i.e., 5 different total rotations for each of the 18 convection runs). We do not formally invoke the age uncertainty of the three shorelines when correcting for DT change. Instead, all DT corrections are based on simulations that ran for 5 Myr, given the limited change in DT that would be expected over the relatively short time span associated with the age uncertainty of the shorelines.

In order to understand how well our DT model fits the spatial variability of the data, we finally calculate the mean squared weighted deviation (MSWD) for each DT model:

$$\mathrm{MSWD}_m = \frac{1}{N}\sum_{i=1}^{N}\left[\frac{(\mathrm{GMSL}_{i,m} - \mathrm{GMSL}_m)^2}{\sigma^2_{\mathrm{GE}_i}}\right]. \tag{7}$$

Given the limited spatial resolution of the tomography models, we do not limit the data-model comparison to only the exact location of the data but sample modeled DT predictions surrounding each site with a maximum distance of 140 km. This distance is comparable to the lateral resolution of our upper mantle tomography models. We then choose the smallest MSWD for each convection-plate rotation pair. A small MSWD signifies that the elevation pattern of the shoreline (i.e., their differential elevations) is matched well by the DT prediction. Specifically, an MSWD of 1 means that the DT prediction is on average 1σ away from the observation. Lastly, our GMSL uncertainty is computed by taking a weighted standard deviation:

$$\sigma_{\mathrm{GMSL}_m} = \sqrt{\frac{\sum_{i=1}^{N} w_i(\mathrm{GMSL}_{i,m} - \mathrm{GMSL}_m)^2}{\sum_{i=1}^{N} w_i}}, \tag{8}$$

where the weights are defined by Equation 5.

In addition to leveraging the GIA-corrected elevations of the three Pliocene shorelines in Argentina, we also draw on additional constraints on present-day DT and bounds of GMSL to further narrow in on the most likely DT models. First, we reject DT models associated with GMSL predictions outside of a realistic range of 10–40 m in the early Pliocene Epoch; this range was conservatively chosen to encompass the wide uncertainty estimates for GMSL during this interval (e.g., Dumitru et al., 2019). Second, we compare our present-day DT predictions to 25 local residual topography measurements and their reported uncertainties (Hoggard et al., 2017). For each DT prediction, we calculate the MSWD (for fits to residual topography) and reject those that yield MSWDs greater than 20. We use the MSWDs that describe how well each convection run fits the deformation pattern in Argentina (Equation 7), as well as these two additional criteria, to identify successful rheological parameters and density structures, and calculate a best estimate of GMSL. We further explore the sensitivity of our best estimate of GMSL to the cutoff values chosen in each of the criteria. As an auxiliary comparison, we compute GMSL in Mallorca, Spain, where analogous, well-mapped early Pliocene sea-level indicators occur (Dumitru et al., 2019). We do so by subtracting our prediction of DT change from the GIA-corrected elevations. We then evaluate the consistency between the GMSL inference computed for Patagonia and Mallorca.

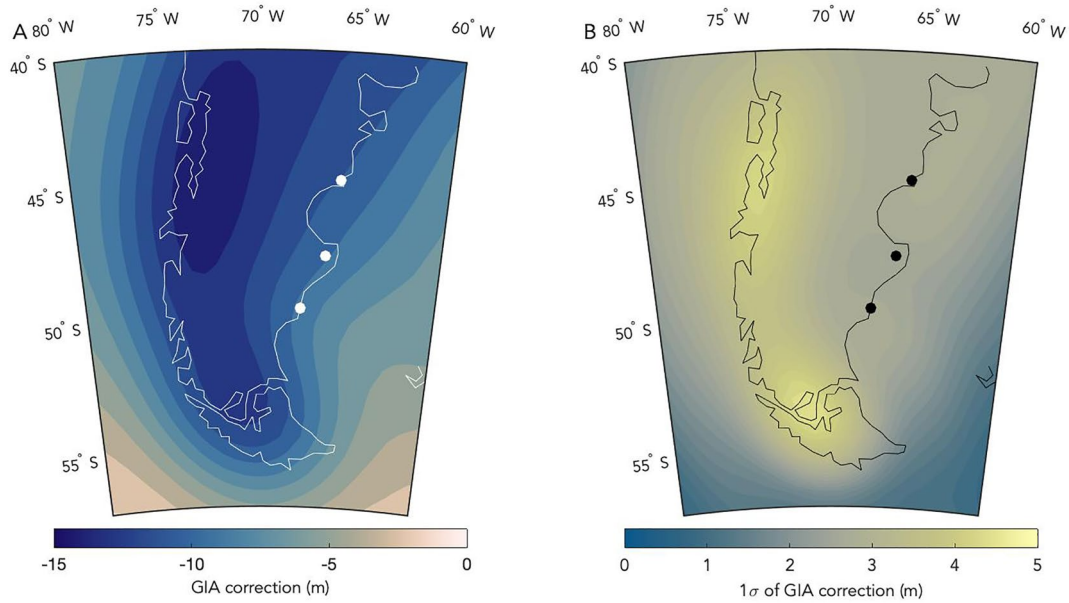

Figure 3. GIA correction and uncertainty. (a) Mean GIA correction for Patagonia from 168 different predictions (24 Earth structures × 7 interglacials). (b) 1σ uncertainty of the GIA correction.

4. Results

4.1. GIA Correction

Ongoing adjustment to ice changes over the last glacial cycle results in a GIA correction that is lowest (most negative) at the center of the Last Glacial Maximum (LGM) Patagonian ice sheet and increases away from it (Figure 3a). This is caused by ice unloading in western Patagonia and the associated solid Earth rebound, which diminishes with distance from the former ice load. In eastern Patagonia, this results in a GIA correction for the three paleoshorelines that varies from −10 to −5 m, which means that this region will continue to uplift by 5–10 m until the solid Earth (and gravity field) has fully equilibrated to ice changes from the last glacial cycle.

Ice sheet variability during the early Pliocene Epoch was predominantly driven by Antarctic ice change, which is associated with a fall in GMSL since that time. The GIA correction associated with this overall ice change is largest in areas of former ice cover (Raymo et al., 2011). Patagonia is far enough away from these ice load changes that adjustment is very similar at each of the three shorelines resulting in a GIA correction that varies from −5 to −2 m. This correction means that local sea level was lower than GMSL due to differential loading of meltwater between oceans and continents (see Raymo et al. (2011) for a detailed discussion). Although we do not explore alternative ice loading histories in this study, our GIA results are likely relatively insensitive to our choice of the ICE-6G_C model for recent disequilibrium and the Pollard et al. (2015)-based model for Pliocene disequilibrium in the far field of major continental ice sheets (e.g., Patagonia). Raymo et al. (2011) performed analogous GIA models for Pliocene disequilibrium using an extension of ICE-5G (Peltier, 2004) for the recent deglaciation and a present-day EAIS and fully deglaciated WAIS and GIS loading history during the Pliocene Epoch. Their models agree with ours in far field regions, and the GIA correction differs by only around 1.5 m in Patagonia. We note that small differences are expected given that their correction is for the mid-Pliocene Epoch, while we focus on the early Pliocene Epoch.

Combining the two GIA corrections yields values of −10.4 ± 2.8 m, −10.5 ± 2.7 m, and −11.4 ± 2.8 m (1σ) at the paleo shoreline locations from south to north (Figure 3). The small differences between these estimates demonstrate that GIA alone cannot explain the large differences in the observed present-day elevations of the three paleoshorelines.

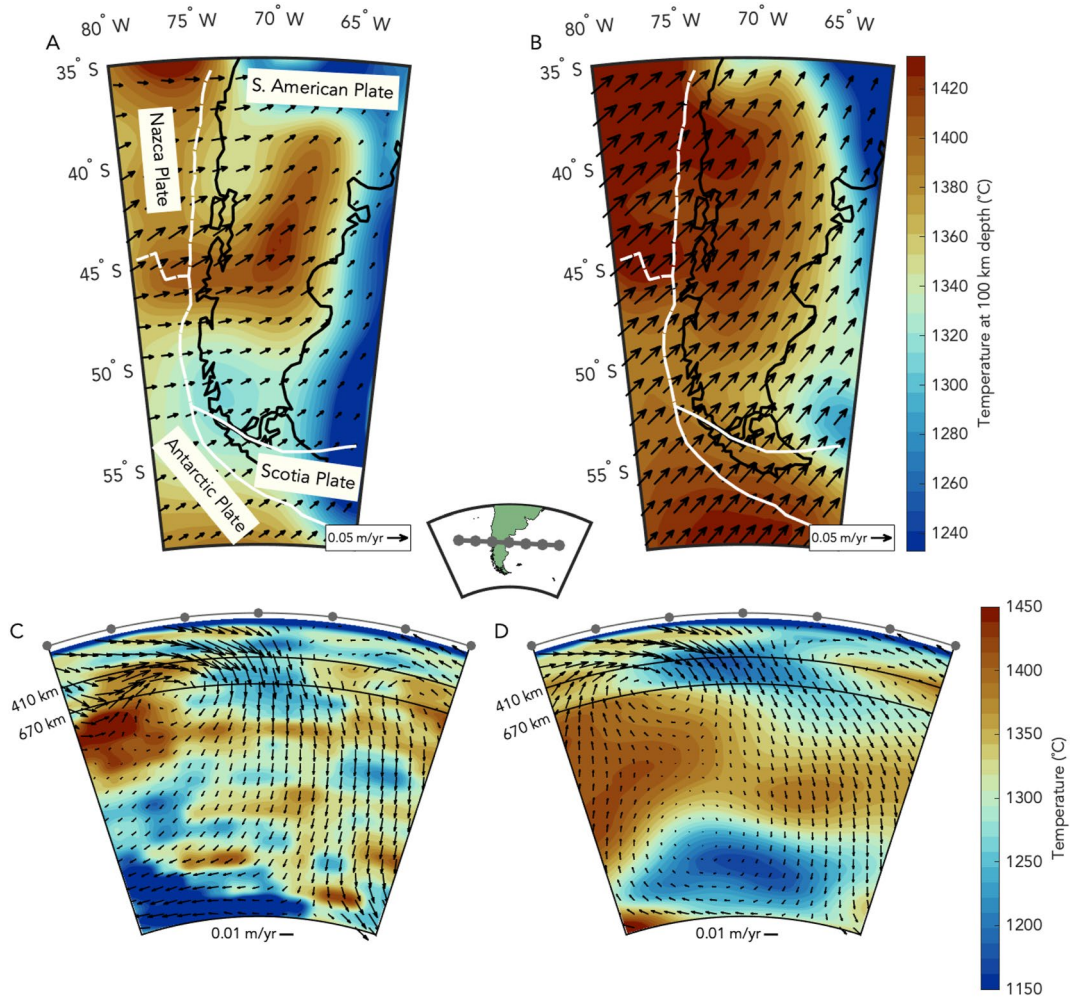

Figure 4. Present-day flow predictions showing inflow of asthenosphere from beneath the Antarctic plate into the Patagonian slab window. (a) Planview mantle flow at 100 km depth initialized with a temperature model computed from the SL2013sv tomography model (Schaeffer & Lebedev, 2013) in the upper mantle. The lower mantle is based on the TX2011 tomography model (Grand, 2002). (b) Same as panel A, but computed from the GLAD-M25 (Lei et al., 2020) tomography model in the upper mantle and S362ANI + M tomography model (Moulik & Ekström, 2014) in the transition zone and lower mantle. (c and d) Same model as in panels a and b, respectively, plotted in cross section from west to east (see map inset for location) and from the surface to the CMB.

4.2. Mantle Flow Simulations

4.2.1. Mantle Temperature and Viscosity

The geometry of the slab window varies across our temperature model suite due to differences in the tomographic models. Temperatures converted from both the SL2013sv and GLAD-M25 models predict warm temperatures corresponding to the slab window that extend over a broad north-south spatial range (~38 to 50°S), which is a larger extent than has been imaged in the ANT-20 model, which is expected since ANT-20 is a full waveform, regional model (Lloyd et al., 2020). Seismic wave speeds from ANT-20 were not converted to temperature as this model has not yet been calibrated for our upper mantle conversion method. SL2013sv results in warm temperatures that cross the Andes at the Chile Triple Junction (CTJ) and extend north under the continent (Figure 4a). Features in GLAD-M25 are similar but clearly broader and local structure may be under-resolved (Figure 4b). The depth extent of relatively warm (above 1,333°C reference temperature) slab-window asthenosphere also varies by tomography model: SL2013sv images inflowing asthenosphere that extends to approximately 250 km depth, while GLAD-M25 extends slightly deeper to approximately 300 km. Temperatures within the slab window peak around 1,370 to 1,420°C at 100 km depth (Figures 4a and 4b). Our suite of temperature

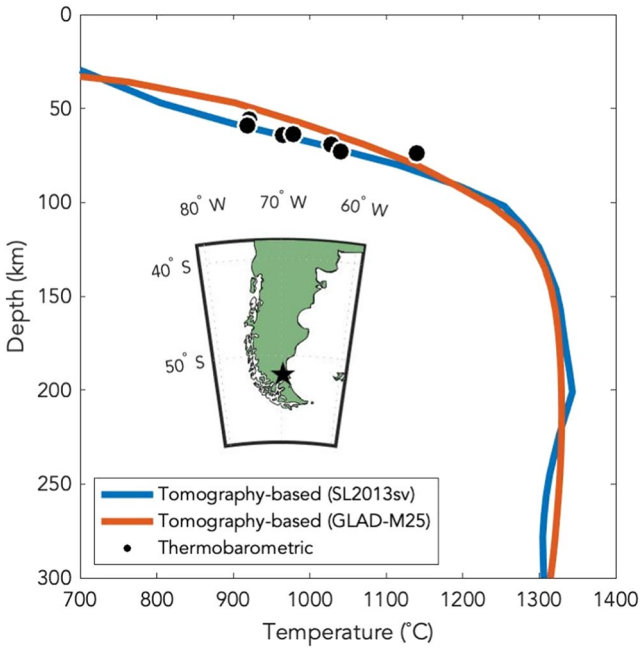

Figure 5. Thermobarometric estimates of mantle xenoliths (black points) that erupted in the Pali-Aike Volcanic Field (star in inset) over Plio-Quaternary times. These estimates of shallow mantle temperatures and pressures agree with local temperature models independently calculated from tomographic models. The blue and red profiles show the depth variations in temperature from a SL2013sv and GLAD-M25-derived upper mantle models, respectively.

models agrees with shallow (50–80 km) thermobarometric calculations of local pressures and temperatures from Plio-Quaternary xenoliths erupted from the Pali-Aike Volcanic Field (Figure 5). Our temperature fields are also generally consistent with the WINTERC-G temperature model (Fullea et al., 2021), which shows local incompressible temperatures around ~1,350 ± 50°C in the upper mantle. This model, which inverted seismic waveforms, satellite gravity measurements, surface elevation, and heat flow data using a self-consistent thermodynamic framework, shows a hot mantle anomaly at 200 km depth that transitions to colder temperatures by 260 km. The slab geometry that has been imaged in WINTERC-G is more similar to that of SL2013sv, compared to GLAD-M25, which defines a more diffuse structure (Fullea et al., 2021). Further, An et al. (2015) have produced temperature estimates beneath the Antarctic plate based on laboratory and seismological constraints of anharmonicity and anelasticity of olivine using the conversion from Goes et al. (2000), and their temperature estimates fall in the middle of our two estimates from SL2013sv and GLAD-M25 in the overlapping regions, mostly under the Southern Ocean. Agreement between these local and spatially continuous independent estimates of mantle temperatures provides support for the seismic velocity-to-temperature conversion methodology in the shallow mantle. The subducted Nazca slab resides at around 450 km with cooler temperatures, varying from 1,175 to 1,250°C (Figures 4c and 4d). In the lower mantle, local structure consists of two dominant regions (~660–1,800 km and ~1,800–2,900 km) of relatively warm and cold temperatures, respectively (Figures 4c and 4d). In general, temperature models mapped from the TX2011 tomography model in the lower mantle reflect the shortest wavelength temperature variability, while those derived from S362ANI + M show broad long wavelength structure; S40RTS-derived models represent an intermediate wavelength structure in the lower mantle.

Our temperature fields lead to viscosity variations of ±1 order of magnitude from our reference profiles (Figures 2b and 2c). Within the slab window we compute lowest viscosities of 3×10^{20} to 4×10^{20} Pa s at 300 km depth. We compute higher viscosities in the transition zone (at 450 km depth) of 4×10^{21} to 5×10^{21} Pa s (Figure 2b). These viscosity variations possibly underestimate the true variability but this smaller range was chosen to ease numerical convergence and reduce computation time.

4.2.2. Mantle Flow

The temperature and corresponding 3-D viscosity models are used to produce predictions of mantle flow. Although our reverse-advection simulations do not include conduction, using a typical conductivity for mantle materials of 10^{-6} m s^{-2}, we calculate a Rayleigh number of 1.31×10^7 for our model based on volume-averaged quantities. In detail, our models show that warm temperatures and low viscosities beneath the Antarctic plate promote inflow of hot asthenosphere through the slab window (Figure 4)—an established slab window mantle flow pattern that has been studied in both laboratory and field settings (e.g., Guillaume et al., 2010; Thorkelson et al., 2011). In the transition zone, colder and stiffer material is downwelling, which when combined with overlying westerly inflow, produces a north-south axial convection cell in the upper half of the mantle (Figures 4c and 4d). This flow scheme is ubiquitous across the suite of convection simulations, despite notable differences in initial temperature structures. The cross section at ~100 km depth shows flow velocities from models that include SL2013sv-derived upper mantle structure also reflect inflow from beneath the Antarctic plate and exhibit a weakly to moderately developed toroidal component, as mantle material flows east then northward along the southern boundary of the subducting Nazca slab (Figure 4a). Recent results from surface wave azimuthal anisotropy, which are sensitive to depths of ~100 km, agree with our prediction of westerly inflow through the slab window and toroidal circulation northward, which is seen in some of our simulations (Figure 4a; Ben-Mansour et al., 2022). Similar dynamics have been observed in other slab window settings (e.g., Western U.S.), where slab rollback has directed toroidal inflow through the window (Zandt & Humphreys, 2008).

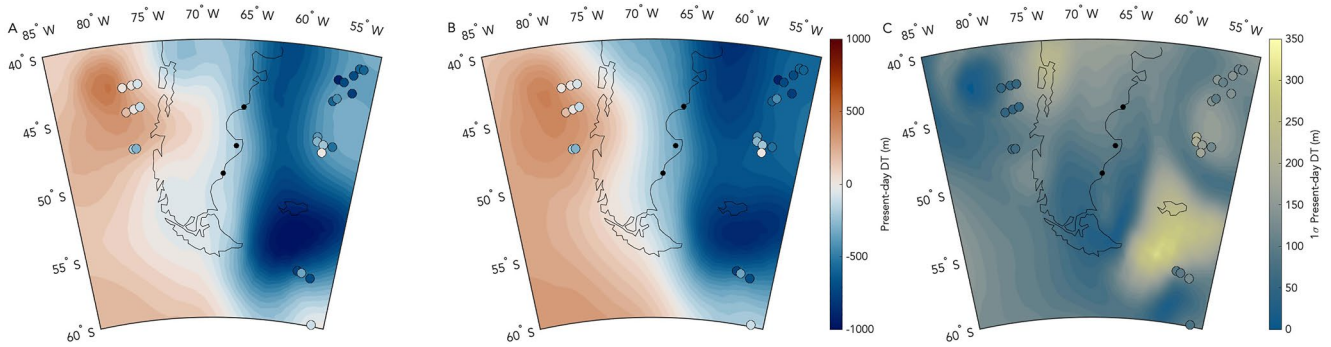

Figure 6. Present-day DT and residual topography measurements. (a) Best fitting present-day DT with SL2013sv upper mantle and TX2011 transition zone and lower mantle-derived structure (Grand, 2002; Schaeffer & Lebedev, 2013). This model uses the V2 viscosity profile. Colored circles show residual topography measurements from Hoggard et al. (2017). (b) Mean present-day DT prediction from entire convection suite. (c) 1σ uncertainty of present-day DT and residual topography measurements (circles).

In the mantle transition zone, our convection models predict downwelling of the relatively cold and high viscosity structure associated with the relict Nazca slab; however, flow slows across the 660 km discontinuity due to a general increase in viscosity. Global geochemical, geodynamic, and geophysical evidence indicates that the transition zone acts as a heterogeneous boundary, where upwellings more easily penetrate than downwellings, with periodic "avalanches" of cold material facilitating exchange (Behn et al., 2004; Gautheron & Moreira, 2002; Meyzen et al., 2007; Tackley et al., 1994). The endothermic phase transition from ringwoodite (or similar compositions) to bridgmanite plays a key role in hampering slab descent (e.g., Bina et al., 2001; Chanyshev et al., 2022; Faccenda & Dal Zilio, 2017; Goes et al., 2017). Our mantle temperature and viscosity models reflect these dynamics as the presence of the geometrically diffuse formerly subducted Nazca slab may suggest temporary slab stagnation or ponding in the transition zone. In general, slab dynamics in the transition zone have the capacity to modulate the extent of uplift at the surface. As such, beneath Patagonia the predicted slab stagnation appears to hamper overall downwelling that might otherwise counteract uplift driven by overlying low viscosity throughflow from beneath the Antarctic plate (Figures 4c and 4d).

4.2.3. Present-Day Dynamic Topography

The best-fitting (described in detail in Section 5.1) DT change solution corresponds to a present-day prediction derived from SL2013sv upper mantle and TX2011 transition zone and lower mantle structure paired with the V2 viscosity profile. The resulting flow field produces a positive topographic anomaly in the South Pacific that extends across the Patagonian continent at the latitude of the slab window, 45° to 50°S, before transitioning to a negative DT signal in the South Atlantic Ocean (Figure 6a). This asymmetric pattern occurs systematically across the convection suite. The positive DT signature over the South Pacific reflects hot, buoyant mantle upwelling associated with the Nazca-Antarctic Ridge. Off the eastern coast, our negative DT predictions coincide with the Argentine Abyssal Plain, a 2,000 km-wide region of anomalously deep bathymetry that has been hypothesized to be one of the largest convective drawdowns on Earth (Hoggard et al., 2016; Hohertz & Carlson, 1998). While our preferred model predicts positive present-day DT directly overlying the slab gap, the eastern coast sits between these two regions of positive and negative DT and as such represents an active geodynamic setting (Figure 6a). The longitudinal pattern reflects a more symmetric arc that peaks near 46°S, which is in agreement with the present-day DT results from Flament et al. (2015). The mean present-day DT prediction yields a similar asymmetrical spatial pattern from west to east, but unlike the preferred solution, it predicts a more diffuse positive anomaly that transitions to negative present-day DT at about 70°W (Figures 6a and 6b), comparable to the residual topography results by Ávila and Dávila (2020).

Since our simulations treat the oceanic lithosphere as neutrally buoyant, we can compare our predictions to the local residual topography estimates from Hoggard et al. (2017), which were obtained by removing the ocean cooling trend from the observed topography (in addition to crustal, sedimentary loading, and geoid corrections). Despite some sign disagreement over the Nazca and Antarctic plates to the west where the residual topography estimates may begin to be contaminated by flexure of the down-going plate beneath the Andean subduction zone, the models and the local residual topography data agree to first order, in particular over the Argentine

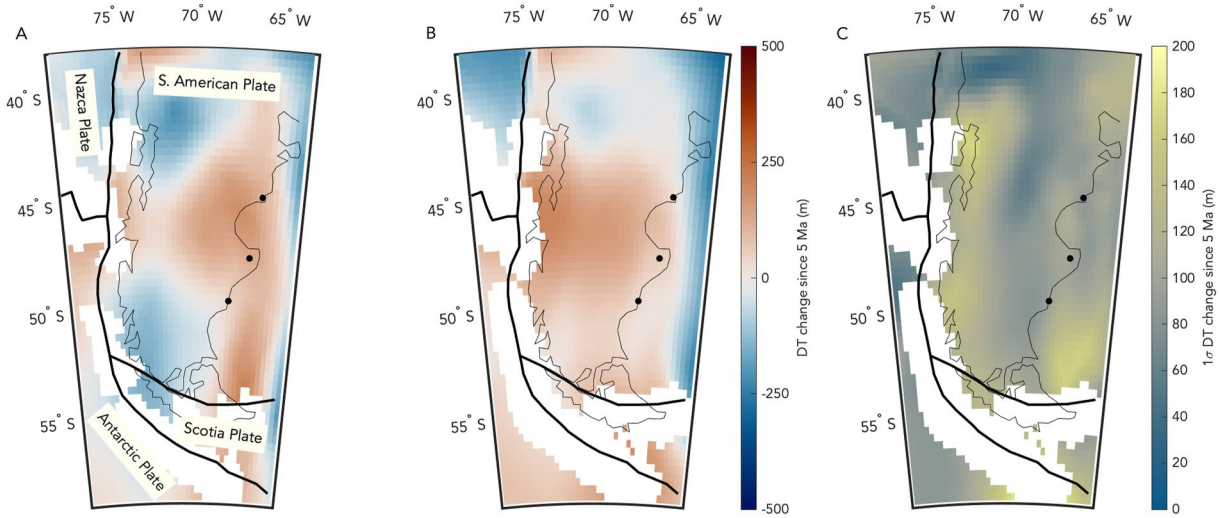

Figure 7. Change in DT predictions across Patagonian foreland. (a) Best-fitting (lowest MSWD) change in DT since the early Pliocene Epoch. This solution uses a mantle temperature model calculated from TX2011 (Grand, 2002) seismic velocities in the transition zone and lower mantle, and SL2013 (Schaeffer & Lebedev, 2013) in the upper mantle. White-out area reflects regions where the crust that has either been formed or subducted since 5 Ma, due to the rotation of tectonic plates over the 5-Myr model timespan. (b) The mean DT change for the full convection suite. (c) 1σ uncertainty from the mean prediction in (b).

Abyssal Plain, where negative residual topography has been mapped (Figures 6a and 6b) and the mantle is downwelling due to the presence of the cold, remnant Nazca slab residing in the mantle transition zone (Figures 4c and 4d). Divergence in data-model comparison likely stems from tomographic inaccuracies and locally important anomalies in lithospheric thickness, which we do not capture in our convection models. While our model suite systematically captures this asymmetrical DT pattern across the region, the models that include upper mantle structure from SL2013sv, instead of GLAD-M25, achieve better fits to the residual topography measurements (see Section 5.1).

4.2.4. Dynamic Topography Change

The change in DT that results from our suite of time-evolving mantle flow models varies from >300 m of uplift to >100 m of subsidence across the eastern coast of Patagonia. The mean DT change prediction of the full suite, however, is characterized by a broad region of positive uplift across the foreland (Figure 7b). Some models also predict uplift to the southeast of the slab window (e.g., Figure 7a), but this anomaly remains untested due to the absence of regional DT change observations. While the mean of our DT change predictions indicates uplift across the eastern coast (Figure 7b), the associated uncertainties at the three paleoshorelines are prohibitively large (22.3 ± 104.1 m, 105.2 ± 102.7 m, and −5.1 ± 98.4 m, 1σ from south to north) to employ as a correction and as such preclude a meaningful inference of GMSL (Figure 7c). In Section 3.3, we leverage additional data to isolate best-fitting models that ultimately can be used as DT change corrections, enabling an inference of GMSL. We found that this step was crucial for robustly correcting shoreline elevations for DT change.

From south to north, our models predict variable DT change (Figure 8). Profiles along the eastern coast through the three shorelines show that the majority of models produces a broad, arc-shaped pattern of DT change with the peak centered on the middle site (Figure 8). Note that our sampling procedure contributes to this similarity in shape, as we select from sites that best fit the differential elevations of the shorelines (see Section 3.2). As such, 50 out of 90 of our DT change models predict an MSWD misfit to the three shorelines of lower than 5. Many of these low-MSWD models predict significant subsidence (Figure 8), however, which is physically unlikely as it would imply sea level in the early Pliocene Epoch was lower than today. In spite of this wide range, several models, which represent the uplift histories most consistent with geodynamic observables (see Section 3.3), fall in an intermediate range while also achieving good fits to the GIA-corrected shoreline elevations (Figure 8).

Past studies have suggested that the Patagonian slab window is a likely setting for ongoing dynamic uplift, which we confirm here (Dávila & Lithgow-Bertelloni, 2013; Dávila et al., 2019; Flament et al., 2015; Guillaume et al., 2009, 2010, 2013). Flament et al. (2015) modeled time-dependent flow, and their most recent DT change predictions (~10 Ma to present) generally agree with our suite of DT change scenarios, indicating broad regional

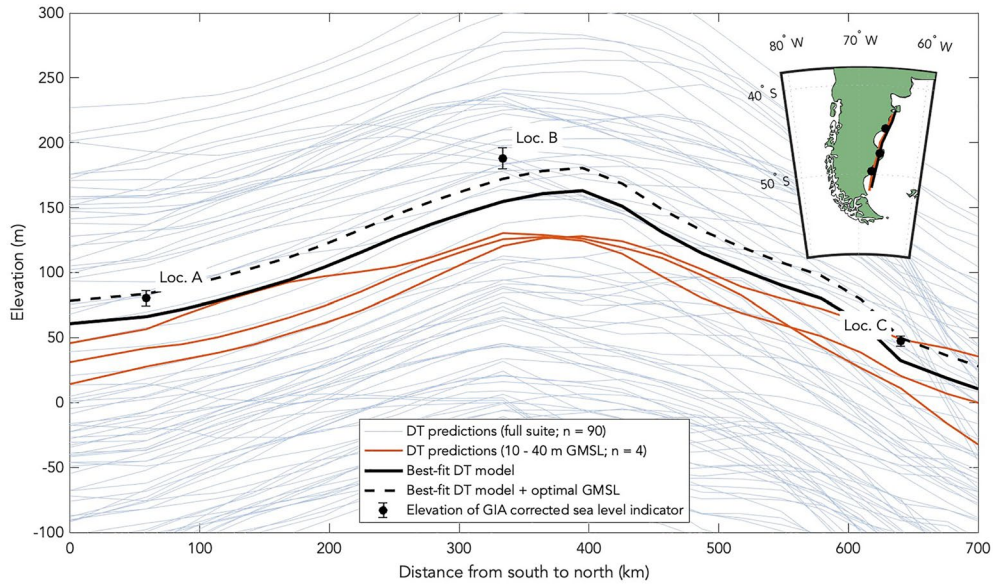

Figure 8. Great circle profiles of DT change across the Patagonian foreland from south to north through the three sea level indicator sites. GIA-corrected elevations are shown by black markers (uncertainties are 1σ). Red profiles show DT change predictions that lead to global mean sea level (GMSL) estimates within 10–40 m. While these predictions correspond to more realistic GMSLs, many achieve poor fits to the GIA-corrected shoreline elevations. The best fitting model is shown in black and its associated sea level prediction including GMSL inference is shown as the black dashed line. Map indicates great circle paths of the preferred models.

uplift across the Patagonian foreland. Trench-parallel tilted fluvial terraces located north and south of ∼46.5°S are among limited geomorphological evidence of DT change in Patagonia that have been used to ground truth models. Separately, Guillaume et al. (2009) and Flament et al. (2015) used these features to validate geodynamic models of northward migration of the CTJ during the Miocene. As these terraces and their tilting predate the time range of our convection models, we cannot comment on their initial tilting history; however, our DT change predictions, which span a time interval over which the CTJ has remained stable (Breitsprecher & Thorkelson, 2009), would drive no additional overprinting of these structures as is consistent with current field mapping (Guillaume et al., 2009). Our DT change predictions may, however, explain northward tilting of Pleistocene marine terraces mapped by Pedoja et al. (2011) located along the eastern coast of Argentina north of our study area, as our models show a positive anomaly extending from the northernmost early Pliocene shoreline transitioning to increasingly negative DT change farther north (Figures 7a and 7b). That said, our models do not target DT change over the Pleistocene and should be compared to these observations cautiously.

5. Discussion

5.1. Best Fitting Earth Model

In Section 4, we describe how our model predictions compare to various observations in isolation. Here, we now seek to investigate which Earth structure performs best in matching all observations simultaneously. In addition to the MSWD, which provides a metric for how well a specific Earth model fits the variation in GIA-corrected elevations of the three paleoshorelines, we use the following screening criteria: (a) the GMSL prediction is limited to a range of 10–40 m; and (b) the misfit to local residual topography measurements (MSWD) has to be less than 20. Only 4 of the 90 total predictions satisfy the constraint of yielding GMSL between 10 and 40 m (Figure 6). Restricting the total suite to those predictions that have an MSWD misfit to local residual topography measurements of less than 20 results in 65 models. Only 1 of the 90 models satisfies both of these constraints simultaneously. This model also predicts a GMSL in Mallorca and Patagonia within 5 m of agreement. This model consists of TX2011-derived transition zone and lower mantle structure and SL2013sv-derived upper mantle structure paired with the V2 viscosity profile, representing the single best convection parameterization within the suite. This best-fitting (MSWD = 1.54) DT change field used a total rotation of 1.8° (0.36° Myr^{-1} × 5 Myr). Notably,

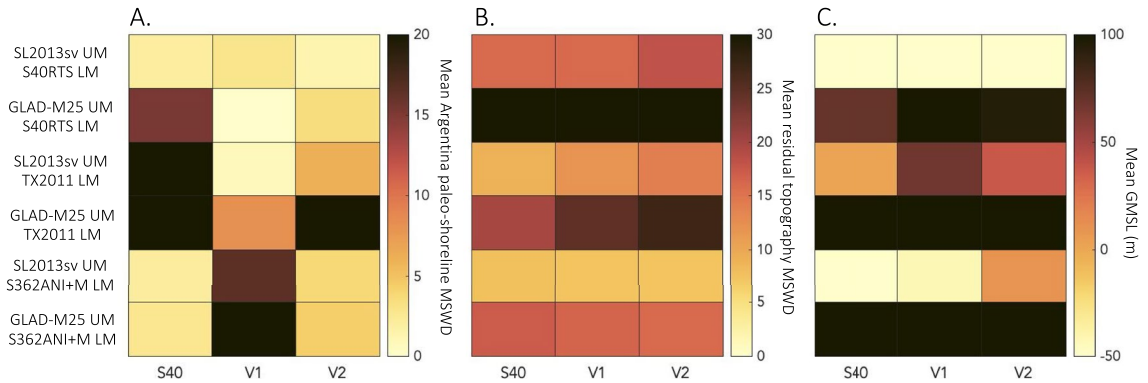

Figure 9. Analysis of temperature and viscosity model parameterization. (a) Heatmap of the mean MSWD that describes how well each convection simulation matches the differential elevations of the paleoshorelines. (b) Heatmap of the mean MSWD describing the fit between the predicted and observed residual topography. Note that a low MSWD indicates a better fit. (c) Mean global mean sea level prediction for each simulation (based on results for the 5 different total lithospheric rotation values).

Steinberger (2016) used several different tomography-derived mantle structures to predict present-day geodynamic observables and also found that a combination of SL2013sv and TX2011 had the greatest success.

In addition to identifying preferred Earth structure from the best-fitting prediction, we consider the success of convection parameters of the entire suite by computing the mean (averaged over the plate rotations) MSWD of each viscosity-temperature model pair for fits to both the three shorelines in Argentina and local residual topography measurements. This reveals that the V1 viscosity profile paired with GLAD-M25 upper mantle and S40RTS transition zone and lower mantle structure achieves the best mean fit to the differential elevations of the three shorelines in Argentina (Figure 9a). That said, this temperature model fails to achieve a good fit (mean MSWD >20) to local residual topography measurements for all three viscosity profiles (Figure 9b). The only temperature model that achieves low mean MSWD (<∼10) fits for the three paleoshorelines in Argentina across all three viscosity profiles is the SL2013sv upper mantle and S40RTS transition zone and lower mantle-derived model (Figure 9a). Models with SL2013sv-derived upper mantle structure systematically correspond to better MSWD fits with local residual topography measurements in comparison with those that include GLAD-M25-derived upper mantle structure (Figure 9b). In addition to their success in fitting observations of present-day DT and DT change, SL2013sv-based convection simulations also prove better at reproducing toroidal flow that has been constrained by surface wave azimuthal anisotropy (Ben-Mansour et al., 2022). This likely reflects the higher resolution of SL2013sv compared to GLAD-M25, which may be attributed to its use of shorter period surface wave data. Lastly, a systematic preference for the mantle viscosity structure remains elusive, likely due to the close similarity amongst the three profiles tested (Figure 2a).

5.2. GMSL Inference

After correcting the observed elevations for GIA and DT change since the early Pliocene Epoch, the remaining offset between the model and the corrected elevations reflects GMSL during the time of deposition. The best-fitting DT change solution (lowest MSWD for the shoreline) yields a GMSL of 17.5 ± 6.4 m. This uncertainty is driven by uncertainties in the GIA correction, the measurement uncertainty, and variability across the three sites (Equation 8). This GMSL value falls within the lower bounds of the uncertainty of the GMSL estimate from Mallorca, Spain where a GMSL of 25.1 m (10.6–28.3 m 16th and 84th uncertainty bounds) was inferred from a sea-level indicator dated to 4.39 ± 0.39 Ma (Dumitru et al., 2019). Using just the northernmost Patagonian shoreline, Rovere et al. (2020) reported a GMSL of 28.4 ± 11.7 m. An estimate of GMSL of 23.4 ± 35.8 m (mean, 1σ) from sea level indicators from South Africa was corrected for GIA and DT change (Hearty et al., 2020; Rovere et al., 2020). The large uncertainties in both of these estimates stem from DT corrections that were not constrained by local observations. In South Africa in particular, this correction is expected to be challenging due to the Large Low-Shear-Velocity Province (LLSVP) which directly underlies this part of the globe at the CMB. This geodynamic structure has uncertain internal compositional heterogeneity and vertical extent, making it difficult to accurately parameterize within convection simulations (Richards et al., 2021). While sensitivity of DT to mantle flow decreases with depth (e.g., Colli et al., 2016), long-wavelength features, such as LLSVPs, may still have a non-negligible impact on DT change over the last 5 Myr.

We test the sensitivity of our final GMSL estimate to the residual topography screening criterion above by adjusting the aforementioned thresholds. We find that relaxing the MSWD threshold for local residual topography from 20 to 30 satisfies 10 additional simulations. However, none of these additional models satisfy our criteria that GMSL must fall within 10–40 m. Additionally, we calculate GMSL for the best-fitting DT change solution but with an ocean water loading amplification based on a 71 km-thick lithosphere (see Section 3.2). This yields a GMSL of 13.4 ± 6.3 m, which falls within the range of the preferred inference of 17.5 ± 6.4 m based on a 90 km-thick lithosphere.

In an early Pliocene climate context, when global mean temperatures were ∼4°C higher than they are today, a GMSL of 17.5 ± 6.4 m (1σ) would require the absence of large sectors of Earth's modern ice sheets. The Greenland Ice Sheet (GIS) was likely small during this time period accounting for around 6–7 m in GMSL difference between the early Pliocene Epoch and today (Bierman et al., 2016). Thermal expansion may explain an additional 1.5 m (Dumitru et al., 2019). This leaves approximately 9.5 ± 6.9 m of additional GMSL, which must be sourced from Antarctica, likely coming from the WAIS and marine-based sectors of the EAIS.

6. Conclusion

We employ the latest results from seismic tomography, rheological mapping, and numerical mantle convection modeling to predict DT changes of 30–150 m along the eastern Patagonia margin. We find that DT change can explain the different elevations of three sea-level indicators supporting the hypothesis that mantle convection plays a major role in deforming Pliocene paleoshorelines (Rovere et al., 2014; Rowley et al., 2013). Our models indicate dynamic upwarping driven primarily by a well-developed north-south axial circulation cell across the slab window that delivers hot asthenosphere from beneath the Antarctic plate through a slab window. The lower branch of the cell is driven by subducting Nazca slab, which might be ponding near the 670 km discontinuity. Shallow (∼100 km) tangential flow is characterized by a toroidal component located in the vicinity of 45°S, 72°W that is in agreement with constraints from surface wave anisotropy (Ben-Mansour et al., 2022).

We constrain the flow pattern to match the deformation observed along the Patagonian margin at the three shorelines and apply additional criteria to identify the most likely flow field and magnitude of deformation. Without applying these constraints, DT predictions vary by >400 m, which highlights their sensitivity to small changes in the parameters used in the convection modeling. This finding implies that studies that use a limited set of convection models that are not constrained by additional local observations can lead to erroneous results. Instead, we provide data-constrained model predictions of DT change and its uncertainty to improve GMSL estimates from the early Pliocene Epoch.

We find that models with an upper mantle structure derived from SL2013sv (Schaeffer & Lebedev, 2013) combined with a transition zone and lower mantle structure from TX2011 (Grand, 2002) yield the best fit to observations, in line with previous work that focused on present-day DT (Richards et al., 2020; Steinberger, 2016). Correcting shorelines for GIA and DT yields a best GMSL estimate of 17.5 ± 6.4 m above present-day for the early Pliocene Epoch, an interval when temperatures and CO_2 were significantly higher than today (Fedorov et al., 2013; Pagani et al., 2010; Seki et al., 2010). This estimate overlaps with that from Mallorcan speleothem records and provides mounting evidence that early Pliocene sea level was significantly higher than today, making it an important calibration target for ice sheet models.

Data Availability Statement

The sea-level code and ice history input used in the GIA modeling is available on Github: https://github.com/ahollyday/SLcode/blob/master/SL_equation_viscoelastic_GIAonly_Pliocene_gcubed.m. The ice history files (see README) are archived on Zenodo. ASPECT (version 2.2.0) that was used to perform the mantle convection modeling is available on Github (https://github.com/ahollyday/aspect/tree/g_cubed_2022, Bangerth, Dannberg, Gassmoeller, & Heister, 2020). The necessary inputs, including initial temperature, viscosity, and LAB extent files, are also archived on Zenodo. An example parameter file is included. The best-fitting DT change (over the past 5 Myr) and the associated present-day DT fields as well as the mean GIA correction and standard deviation are available on Zenodo. All files archived on Zenodo can be found here: https://doi.org/10.5281/zenodo.7508208.

Acknowledgments
We acknowledge computing resources from Columbia University's Shared Research Computing Facility project, which is supported by NIH Research Facility Improvement Grant 1G20RR03893-01, and associated funds from the New York State Empire State Development, Division of Science Technology and Innovation (NYSTAR) Contract C090171, both awarded 15 April 2010. We thank the Computational Infrastructure for Geodynamics (geodynamics.org) which is funded by the National Science Foundation under award EAR-0949446 and EAR-1550901 for supporting the development of ASPECT. The authors acknowledge PALSEA, a working group of the International Union for Quaternary Sciences (INQUA) and Past Global Changes (PAGES), which in turn received support from the Swiss Academy of Sciences and the Chinese Academy of Sciences. JA acknowledges funding from the Alfred P. Sloan Research Fellowship FG-2021-15970. FDR thanks the Imperial College Research Fellowship and Schmidt Science Fellowship schemes. MH acknowledges support from the Australian Research Council DECRA DE220101519 and the Australian Government's *Exploring for the Future* program. AR acknowledges support from the European Research Council (ERC) under the European Union's Horizon 2020 research and innovation programme (grant agreement n. 802414). We thank Nicolas Flament and Federico Dávila for helpful and constructive reviews.

References

An, M., Wiens, D. A., Zhao, Y., Feng, M., Nyblade, A., Kanao, M., et al. (2015). Temperature, lithosphere-asthenosphere boundary, and heat flux beneath the Antarctic Plate inferred from seismic velocities. *Journal of Geophysical Research: Solid Earth*, *120*(12), 8720–8742. https://doi.org/10.1002/2015JB011917

Argus, D. F., Gordon, R. G., & DeMets, C. (2011). Geologically current motion of 56 plates relative to the no-net-rotation reference frame. *Geochemistry, Geophysics, Geosystems*, *12*(11), Q11001. https://doi.org/10.1029/2011GC003751

Austermann, J., & Mitrovica, J. X. (2015). Calculating gravitationally self-consistent sea level changes driven by dynamic topography. *Geophysical Journal International*, *203*(3), 1909–1922. https://doi.org/10.1093/gji/ggv371

Austermann, J., Mitrovica, J. X., Huybers, P., & Rovere, A. (2017). Detection of a dynamic topography signal in last interglacial sea-level records. *Science Advances*, *3*(7), e1700457. https://doi.org/10.1126/sciadv.1700457

Ávila, P., & Dávila, F. M. (2018). Heat flow and lithospheric thickness analysis in the Patagonian asthenospheric windows, southern South America. *Tectonophysics*, *747–748*, 99–107. https://doi.org/10.1016/j.tecto.2018.10.006

Ávila, P., & Dávila, F. M. (2020). Lithospheric thinning and dynamic uplift effects during slab window formation, southern Patagonia (45°–55°S). *Journal of Geodynamics*, *133*, 101689. https://doi.org/10.1016/j.jog.2019.101689

Bangerth, W., Dannberg, J., Gassmoeller, R., & Heister, T. (2020). ASPECT v2.2.0 [Dataset]. Zenodo. https://doi.org/10.5281/zenodo.3924604

Bangerth, W., Dannberg, J., Gassmoeller, R., Heister, T., Myhill, R., & Naliboff, J. (2020). ASPECT: Advanced Solver for Problems in Earth's ConvecTion, user manual. https://doi.org/10.6084/m9.figshare.4865333.v7

Behn, M. D., Conrad, C. P., & Silver, P. G. (2004). Detection of upper mantle flow associated with the African Superplume. *Earth and Planetary Science Letters*, *224*(3), 259–274. https://doi.org/10.1016/j.epsl.2004.05.026

Ben-Mansour, W., Wiens, D. A., Mark, H. F., Russo, R. M., Richter, A., Marderwald, E., & Barrientos, S. (2022). Mantle flow pattern associated with the patagonian slab window determined from azimuthal anisotropy. *Geophysical Research Letters*, *49*(18), e2022GL099871. https://doi.org/10.1029/2022GL099871

Bhanot, K. K., Downes, H., Petrone, C. M., Humphreys-Williams, E., & Clark, B. (2020). Micro-CT investigation of garnet-spinel clusters in mantle peridotite xenoliths. *Lithos*, *352–353*, 105250. https://doi.org/10.1016/j.lithos.2019.105250

Bierman, P. R., Shakun, J. D., Corbett, L. B., Zimmerman, S. R., & Rood, D. H. (2016). A persistent and dynamic East Greenland Ice Sheet over the past 7.5 million years. *Nature*, *540*, 7632–260. https://doi.org/10.1038/nature20147

Bina, C. R., Stein, S., Marton, F. C., & Van Ark, E. M. (2001). Implications of slab mineralogy for subduction dynamics. *Physics of the Earth and Planetary Interiors*, *127*(1), 51–66. https://doi.org/10.1016/S0031-9201(01)00221-7

Breitsprecher, K., & Thorkelson, D. J. (2009). Neogene kinematic history of Nazca–Antarctic–Phoenix slab windows beneath Patagonia and the Antarctic Peninsula. *Tectonophysics*, *464*(1), 10–20. https://doi.org/10.1016/j.tecto.2008.02.013

Burke, K. D., Williams, J. W., Chandler, M. A., Haywood, A. M., Lunt, D. J., & Otto-Bliesner, B. L. (2018). Pliocene and Eocene provide best analogs for near-future climates. *Proceedings of the National Academy of Sciences*, *115*(52), 13288–13293. https://doi.org/10.1073/pnas.1809600115

Chanyshev, A., Ishii, T., Bondar, D., Bhat, S., Kim, E. J., Farla, R., et al. (2022). Depressed 660-km discontinuity caused by akimotoite–bridgmanite transition. *Nature*, *601*, 7891–73. https://doi.org/10.1038/s41586-021-04157-z

Colli, L., Ghelichkhan, S., & Bunge, H.-P. (2016). On the ratio of dynamic topography and gravity anomalies in a dynamic Earth. *Geophysical Research Letters*, *43*(6), 2510–2516. https://doi.org/10.1002/2016GL067929

Collins, M., Knutti, R., Arblaster, J., Dufresne, J.-L., Fichefet, T., Friedlingstein, P., et al. (2013). Long-term climate change: Projections, commitments and irreversibility. In *Climate change 2013: The physical science basis: Contribution of Working Group I to the Fifth Assessment Report of the Intergovernmental Panel on Climate Change* (pp. 1029–1136).

Cook, C. P., van de Flierdt, T., Williams, T., Hemming, S. R., Iwai, M., Kobayashi, M., et al. (2013). Dynamic behaviour of the East Antarctic ice sheet during Pliocene warmth. *Nature Geoscience*, *6*, 9–769. https://doi.org/10.1038/ngeo1889

Czarnota, K., Hoggard, M. J., White, N., & Winterbourne, J. (2013). Spatial and temporal patterns of Cenozoic dynamic topography around Australia. *Geochemistry, Geophysics, Geosystems*, *14*(3), 634–658. https://doi.org/10.1029/2012GC004392

Dalton, C. A., Ekström, G., & Dziewonski, A. M. (2009). Global seismological shear velocity and attenuation: A comparison with experimental observations. *Earth and Planetary Science Letters*, *284*(1–2), 65–75. https://doi.org/10.1016/j.epsl.2009.04.009

Dávila, F., Avila, P., Martina, F., Canelo, H., Nóbile, J., Collo, G., et al. (2019). Measuring dynamic topography in South America (pp. 35–66). https://doi.org/10.1016/B978-0-12-816009-1.00003-4

Dávila, F. M., & Lithgow-Bertelloni, C. (2013). Dynamic topography in South America. *Journal of South American Earth Sciences*, *43*, 127–144. https://doi.org/10.1016/j.jsames.2012.12.002

DeConto, R. M., & Pollard, D. (2016). Contribution of Antarctica to past and future sea-level rise. *Nature*, *531*, 7596–597. https://doi.org/10.1038/nature17145

DeConto, R. M., Pollard, D., Alley, R. B., Velicogna, I., Gasson, E., Gomez, N., et al. (2021). The Paris Climate Agreement and future sea-level rise from Antarctica. *Nature*, *593*, 7857–89. https://doi.org/10.1038/s41586-021-03427-0

del Río, C. J., Griffin, M., McArthur, J. M., Martínez, S., & Thirlwall, M. F. (2013). Evidence for early Pliocene and late Miocene transgressions in southern Patagonia (Argentina): $^{87}Sr/^{86}Sr$ ages of the pectinid "Chlamys" actinodes (Sowerby). *Journal of South American Earth Sciences*, *47*, 220–229. https://doi.org/10.1016/j.jsames.2013.08.004

Dumitru, O. A., Austermann, J., Polyak, V. J., Fornós, J. J., Asmerom, Y., Ginés, J., et al. (2019). Constraints on global mean sea level during Pliocene warmth. *Nature*, *574*, 7777–236. https://doi.org/10.1038/s41586-019-1543-2

Dziewonski, A. M., & Anderson, D. L. (1981). Preliminary reference Earth model. *Physics of the Earth and Planetary Interiors*, *25*(4), 297–356. https://doi.org/10.1016/0031-9201(81)90046-7

Eagles, G. (2004). Tectonic evolution of the Antarctic–Phoenix plate system since 15 Ma. *Earth and Planetary Science Letters*, *217*(1), 97–109. https://doi.org/10.1016/S0012-821X(03)00584-3

Faccenda, M., & Dal Zilio, L. (2017). The role of solid–solid phase transitions in mantle convection. *Lithos*, *268–271*, 198–224. https://doi.org/10.1016/j.lithos.2016.11.007

Fedorov, A. V., Brierley, C. M., Lawrence, K. T., Liu, Z., Dekens, P. S., & Ravelo, A. C. (2013). Patterns and mechanisms of early Pliocene warmth. *Nature*, *496*, 7443–49. https://doi.org/10.1038/nature12003

Fischer, H., Meissner, K. J., Mix, A. C., Abram, N. J., Austermann, J., Brovkin, V., et al. (2018). Palaeoclimate constraints on the impact of 2°C anthropogenic warming and beyond. *Nature Geoscience*, *11*, 7–485. https://doi.org/10.1038/s41561-018-0146-0

Flament, N., Gurnis, M., Müller, R. D., Bower, D. J., & Husson, L. (2015). Influence of subduction history on South American topography. *Earth and Planetary Science Letters*, *430*, 9–18. https://doi.org/10.1016/j.epsl.2015.08.006

Forte, A. M., Peltier, W. R., Dziewonski, A. M., & Woodward, R. L. (1993). Dynamic surface topography: A new interpretation based upon mantle flow models derived from seismic tomography. *Geophysical Research Letters*, *20*(3), 225–228. https://doi.org/10.1029/93GL00249

Forte, A. M., Quéré, S., Moucha, R., Simmons, N. A., Grand, S. P., Mitrovica, J. X., & Rowley, D. B. (2010). Joint seismic–geodynamic-mineral physical modelling of African geodynamics: A reconciliation of deep-mantle convection with surface geophysical constraints. *Earth and Planetary Science Letters*, *295*(3), 329–341. https://doi.org/10.1016/j.epsl.2010.03.017

Fullea, J., Lebedev, S., Martinec, Z., & Celli, N. L. (2021). WINTERC-G: Mapping the upper mantle thermochemical heterogeneity from coupled geophysical–petrological inversion of seismic waveforms, heat flow, surface elevation and gravity satellite data. *Geophysical Journal International*, *226*(1), 146–191. https://doi.org/10.1093/gji/ggab094

Gautheron, C., & Moreira, M. (2002). Helium signature of the subcontinental lithospheric mantle. *Earth and Planetary Science Letters*, *199*(1), 39–47. https://doi.org/10.1016/S0012-821X(02)00563-0

Glišović, P., & Forte, A. M. (2015). Importance of initial buoyancy field on evolution of mantle thermal structure: Implications of surface boundary conditions. *Geoscience Frontiers*, *6*(1), 3–22. https://doi.org/10.1016/j.gsf.2014.05.004

Goes, S., Agrusta, R., van Hunen, J., & Garel, F. (2017). Subduction-transition zone interaction: A review. *Geosphere*, *13*(3), 644–664. https://doi.org/10.1130/GES01476.1

Goes, S., Govers, R., & Vacher, P. (2000). Shallow mantle temperatures under Europe from P and S wave tomography. *Journal of Geophysical Research*, *105*(B5), 11153–11169. https://doi.org/10.1029/1999JB900300

Gorring, M., Singer, B., Gowers, J., & Kay, S. M. (2003). Plio–Pleistocene basalts from the Meseta del Lago Buenos Aires, Argentina: Evidence for asthenosphere–lithosphere interactions during slab window magmatism. *Chemical Geology*, *193*(3), 215–235. https://doi.org/10.1016/S0009-2541(02)00249-8

Grand, S. P. (2002). Mantle shear–wave tomography and the fate of subducted slabs. *Philosophical Transactions of the Royal Society of London. Series A: Mathematical, Physical and Engineering Sciences*, *360*(1800), 2475–2491. https://doi.org/10.1098/rsta.2002.1077

Guillaume, B., Gautheron, C., Simon-Labric, T., Martinod, J., Roddaz, M., & Douville, E. (2013). Dynamic topography control on Patagonian relief evolution as inferred from low temperature thermochronology. *Earth and Planetary Science Letters*, *364*, 157–167. https://doi.org/10.1016/j.epsl.2012.12.036

Guillaume, B., Martinod, J., Husson, L., Roddaz, M., & Riquelme, R. (2009). Neogene uplift of central eastern Patagonia: Dynamic response to active spreading ridge subduction? *Tectonics*, *28*(2), TC2009. https://doi.org/10.1029/2008TC002324

Guillaume, B., Moroni, M., Funiciello, F., Martinod, J., & Faccenna, C. (2010). Mantle flow and dynamic topography associated with slab window opening: Insights from laboratory models. *Tectonophysics*, *496*(1), 83–98. https://doi.org/10.1016/j.tecto.2010.10.014

Guivel, C., Morata, D., Pelleter, E., Espinoza, F., Maury, R. C., Lagabrielle, Y., et al. (2006). Miocene to Late Quaternary Patagonian basalts (46–47°S): Geochronometric and geochemical evidence for slab tearing due to active spreading ridge subduction. *Journal of Volcanology and Geothermal Research*, *149*(3), 346–370. https://doi.org/10.1016/j.jvolgeores.2005.09.002

Haywood, A. M., Hill, D. J., Dolan, A. M., Otto-Bliesner, B. L., Bragg, F., Chan, W.-L., et al. (2013). Large-scale features of Pliocene climate: Results from the Pliocene model intercomparison project. *Climate of the Past*, *9*(1), 191–209. https://doi.org/10.5194/cp-9-191-2013

Hearty, P. J., Rovere, A., Sandstrom, M. R., O'Leary, M. J., Roberts, D., & Raymo, M. E. (2020). Pliocene-Pleistocene Stratigraphy and sea-level estimates, Republic of South Africa with implications for a 400 ppmv CO_2 world. *Paleoceanography and Paleoclimatology*, *35*(7), e2019PA003835. https://doi.org/10.1029/2019PA003835

Heister, T., Dannberg, J., Gassmöller, R., & Bangerth, W. (2017). High accuracy mantle convection simulation through modern numerical methods – II: Realistic models and problems. *Geophysical Journal International*, *210*(2), 833–851. https://doi.org/10.1093/gji/ggx195

Hoggard, M., Austermann, J., Randel, C., & Stephenson, S. (2021). Observational estimates of dynamic topography through space and time. Retrieved from https://eartharxiv.org/repository/view/1997/

Hoggard, M. J., White, N., & Al-Attar, D. (2016). Global dynamic topography observations reveal limited influence of large-scale mantle flow. *Nature Geoscience*, *9*, 6–463. https://doi.org/10.1038/ngeo2709

Hoggard, M. J., Winterbourne, J., Czarnota, K., & White, N. (2017). Oceanic residual depth measurements, the plate cooling model, and global dynamic topography. *Journal of Geophysical Research: Solid Earth*, *122*(3), 2328–2372. https://doi.org/10.1002/2016JB013457

Hohertz, W. L., & Carlson, R. L. (1998). An independent test of thermal subsidence and asthenosphere flow beneath the Argentine Basin. *Earth and Planetary Science Letters*, *161*(1), 73–83. https://doi.org/10.1016/S0012-821X(98)00138-1

Jordan, T. H. (1978). Composition and development of the continental tectosphere. *Nature*, *274*, 5671–548. https://doi.org/10.1038/274544a0

Kendall, R. A., Mitrovica, J. X., & Milne, G. A. (2005). On post-glacial sea level – II. Numerical formulation and comparative results on spherically symmetric models. *Geophysical Journal International*, *161*(3), 679–706. https://doi.org/10.1111/j.1365-246X.2005.02553.x

Kronbichler, M., Heister, T., & Bangerth, W. (2012). High accuracy mantle convection simulation through modern numerical methods. *Geophysical Journal International*, *191*(1), 12–29. https://doi.org/10.1111/j.1365-246X.2012.05609.x

Lay, T., Hernlund, J., & Buffett, B. A. (2008). Core–mantle boundary heat flow. *Nature Geoscience*, *1*, 1–32. https://doi.org/10.1038/ngeo.2007.44

Lei, W., Ruan, Y., Bozdağ, E., Peter, D., Lefebvre, M., Komatitsch, D., et al. (2020). Global adjoint tomography—Model GLAD-M25. *Geophysical Journal International*, *223*(1), 1–21. https://doi.org/10.1093/gji/ggaa253

Lisiecki, L. E., & Raymo, M. E. (2005). A Pliocene-Pleistocene stack of 57 globally distributed benthic $\delta^{18}O$ records. *Paleoceanography*, *20*(1). https://doi.org/10.1029/2004PA001071

Lithgow-Bertelloni, C., & Gurnis, M. (1997). Cenozoic subsidence and uplift of continents from time-varying dynamic topography. *Geology*, *25*(8), 735–738. https://doi.org/10.1130/0091-7613(1997)025<0735:CSAUOC>2.3.CO;2

Livermore, R., Balanyá, J. C., Maldonado, A., Martínez, J. M., Rodríguez-Fernández, J., de Galdeano, C. S., et al. (2000). Autopsy on a dead spreading center: The Phoenix Ridge, Drake Passage, Antarctica. *Geology*, *28*(7), 607–610. https://doi.org/10.1130/0091-7613(2000)28<607:AOADSC>2.0.CO;2

Lloyd, A. J., Wiens, D. A., Zhu, H., Tromp, J., Nyblade, A. A., Aster, R. C., et al. (2020). Seismic structure of the Antarctic upper mantle imaged with adjoint tomography. *Journal of Geophysical Research: Solid Earth*, *125*(3). https://doi.org/10.1029/2019JB017823

Meyzen, C. M., Blichert-Toft, J., Ludden, J. N., Humler, E., Mével, C., & Albarède, F. (2007). Isotopic portrayal of the Earth's upper mantle flow field. *Nature*, *447*(7148), 1069–1074. https://doi.org/10.1038/nature05920

Miller, K. G., Wright, J. D., Browning, J. V., Kulpecz, A., Kominz, M., Naish, T. R., et al. (2012). High tide of the warm Pliocene: Implications of global sea level for Antarctic deglaciation. *Geology*, *40*(5), 407–410. https://doi.org/10.1130/G32869.1

Mitrovica, J. X., & Forte, A. M. (2004). A new inference of mantle viscosity based upon joint inversion of convection and glacial isostatic adjustment data. *Earth and Planetary Science Letters*, *225*(1), 177–189. https://doi.org/10.1016/j.epsl.2004.06.005

Moucha, R., Forte, A. M., Mitrovica, J. X., Rowley, D. B., Quéré, S., Simmons, N. A., & Grand, S. P. (2008). Dynamic topography and long-term sea-level variations: There is no such thing as a stable continental platform. *Earth and Planetary Science Letters*, *271*(1), 101–108. https://doi.org/10.1016/j.epsl.2008.03.056

Moucha, R., & Ruetenik, G. A. (2017). Interplay between dynamic topography and flexure along the U.S. Atlantic passive margin: Insights from landscape evolution modeling. *Global and Planetary Change*, *149*, 72–78. https://doi.org/10.1016/j.gloplacha.2017.01.004

Moulik, P., & Ekström, G. (2014). An anisotropic shear velocity model of the Earth's mantle using normal modes, body waves, surface waves and long-period waveforms. *Geophysical Journal International*, *199*(3), 1713–1738. https://doi.org/10.1093/gji/ggu356

Müller, R. D., Hassan, R., Gurnis, M., Flament, N., & Williams, S. E. (2018). Dynamic topography of passive continental margins and their hinterlands since the Cretaceous. *Gondwana Research*, *53*, 225–251. https://doi.org/10.1016/j.gr.2017.04.028

Naish, T., Powell, R., Levy, R., Wilson, G., Scherer, R., Talarico, F., et al. (2009). Obliquity-paced Pliocene West Antarctic ice sheet oscillations. *Nature*, *458*, 7236–328. https://doi.org/10.1038/nature07867

Nickel, K. G., & Green, D. H. (1985). Empirical geothermobarometry for garnet peridotites and implications for the nature of the lithosphere, kimberlites and diamonds. *Earth and Planetary Science Letters*, *73*(1), 158–170. https://doi.org/10.1016/0012-821X(85)90043-3

Pagani, M., Liu, Z., LaRiviere, J., & Ravelo, A. C. (2010). High Earth-system climate sensitivity determined from Pliocene carbon dioxide concentrations. *Nature Geoscience*, *3*, 1–30. https://doi.org/10.1038/ngeo724

Pedoja, K., Regard, V., Husson, L., Martinod, J., Guillaume, B., Fucks, E., et al. (2011). Uplift of quaternary shorelines in eastern Patagonia: Darwin revisited. *Geomorphology*, *127*(3), 121–142. https://doi.org/10.1016/j.geomorph.2010.08.003

Peltier, W. R. (2004). Global glacial isostasy and the surface of the ice-age Earth: The ICE-5G (VM2) Model and GRACE. *Annual Review of Earth and Planetary Sciences*, *32*(1), 111–149. https://doi.org/10.1146/annurev.earth.32.082503.144359

Peltier, W. R., Argus, D. F., & Drummond, R. (2015). Space geodesy constrains ice age terminal deglaciation: The global ICE-6G_C (VM5a) model. *Journal of Geophysical Research: Solid Earth*, *120*(1), 450–487. https://doi.org/10.1002/2014JB011176

Peltier, W. R., & Fairbanks, R. G. (2006). Global glacial ice volume and Last Glacial Maximum duration from an extended Barbados sea level record. *Quaternary Science Reviews*, *25*(23), 3322–3337. https://doi.org/10.1016/j.quascirev.2006.04.010

Perucca, L., Alvarado, P., & Saez, M. (2016). Neotectonics and seismicity in southern Patagonia. *Geological Journal*, *51*(4), 545–559. https://doi.org/10.1002/gj.2649

Pollard, D., DeConto, R. M., & Alley, R. B. (2015). Potential Antarctic Ice Sheet retreat driven by hydrofracturing and ice cliff failure. *Earth and Planetary Science Letters*, *412*, 112–121. https://doi.org/10.1016/j.epsl.2014.12.035

Priestley, K., McKenzie, D., & Ho, T. (2018). A lithosphere–asthenosphere boundary—A global model derived from multimode surface-wave tomography and petrology. In *Lithospheric discontinuities* (pp. 111–123). American Geophysical Union. https://doi.org/10.1002/9781119249740.ch6

Raymo, M. E., Kozdon, R., Evans, D., Lisiecki, L., & Ford, H. L. (2018). The accuracy of mid-Pliocene $\delta^{18}O$-based ice volume and sea level reconstructions. *Earth-Science Reviews*, *177*, 291–302. https://doi.org/10.1016/j.earscirev.2017.11.022

Raymo, M. E., Mitrovica, J. X., O'Leary, M. J., DeConto, R. M., & Hearty, P. J. (2011). Departures from eustasy in Pliocene sea-level records. *Nature Geoscience*, *4*(5), 328–332. https://doi.org/10.1038/ngeo1118

Richards, F., Hoggard, M. J., Ghelichkhan, S., Koelemeijer, P., & Lau, H. (2021). Geodynamic, geodetic, and seismic constraints favour deflated and dense-cored LLVPs. Retrieved from https://eartharxiv.org/repository/view/2465/

Richards, F. D., Hoggard, M. J., White, N., & Ghelichkhan, S. (2020). Quantifying the relationship between short-wavelength dynamic topography and thermomechanical structure of the upper mantle using calibrated parameterization of anelasticity. *Journal of Geophysical Research: Solid Earth*, *125*(9), e2019JB019062. https://doi.org/10.1029/2019JB019062

Ritsema, J., Deuss, A., van Heijst, H. J., & Woodhouse, J. H. (2011). S40RTS: A degree-40 shear-velocity model for the mantle from new Rayleigh wave dispersion, teleseismic traveltime and normal-mode splitting function measurements. *Geophysical Journal International*, *184*(3), 1223–1236. https://doi.org/10.1111/j.1365-246X.2010.04884.x

Rodriguez, J. F. R., & Littke, R. (2001). Petroleum generation and accumulation in the Golfo San Jorge Basin, Argentina: A basin modeling study. *Marine and Petroleum Geology*, *18*(9), 995–1028. https://doi.org/10.1016/S0264-8172(01)00038-1

Rohling, E. J., Foster, G. L., Grant, K. M., Marino, G., Roberts, A. P., Tamisiea, M. E., & Williams, F. (2014). Sea-level and deep-sea-temperature variability over the past 5.3 million years. *Nature*, *508*, 7497–482. https://doi.org/10.1038/nature13230

Rovere, A., Pappalardo, M., Richiano, S., Aguirre, M., Sandstrom, M. R., Hearty, P. J., et al. (2020). Higher than present global mean sea level recorded by an Early Pliocene intertidal unit in Patagonia (Argentina). *Communications Earth & Environment*, *1*, 1. https://doi.org/10.1038/s43247-020-00067-6

Rovere, A., Raymo, M. E., Mitrovica, J. X., Hearty, P. J., O'Leary, M. J., & Inglis, J. D. (2014). The Mid-Pliocene sea-level conundrum: Glacial isostasy, eustasy and dynamic topography. *Earth and Planetary Science Letters*, *387*, 27–33. https://doi.org/10.1016/j.epsl.2013.10.030

Rowley, D. B., Forte, A. M., Moucha, R., Mitrovica, J. X., Simmons, N. A., & Grand, S. P. (2013). Dynamic topography change of the eastern United States since 3 million years ago. *Science*, *340*(6140), 1560–1563. https://doi.org/10.1126/science.1229180

Russo, R. M., Luo, H., Wang, K., Ambrosius, B., Mocanu, V., He, J., et al. (2022). Lateral variation in slab window viscosity inferred from global navigation satellite system (GNSS)–observed uplift due to recent mass loss at Patagonia ice fields. *Geology*, *50*(1), 111–115. https://doi.org/10.1130/G49388.1

Sachse, V. F., Anka, Z., Littke, R., Rodriguez, J. F., Horsfield, B., & di Primio, R. (2016). Burial, temperature and maturation history of the Austral and western Malvinas basins, southern Argentina, based on 3D basin modelling. *Journal of Petroleum Geology*, *39*(2), 169–191. https://doi.org/10.1111/jpg.12639

Sandiford, M. (2007). The tilting continent: A new constraint on the dynamic topographic field from Australia. *Earth and Planetary Science Letters*, *261*(1), 152–163. https://doi.org/10.1016/j.epsl.2007.06.023

Schaeffer, A. J., & Lebedev, S. (2013). Global shear speed structure of the upper mantle and transition zone. *Geophysical Journal International*, *194*(1), 417–449. https://doi.org/10.1093/gji/ggt095

Scherer, R. P., DeConto, R. M., Pollard, D., & Alley, R. B. (2016). Windblown Pliocene diatoms and East Antarctic ice sheet retreat. *Nature Communications*, *7*, 1. https://doi.org/10.1038/ncomms12957

Seki, O., Foster, G. L., Schmidt, D. N., Mackensen, A., Kawamura, K., & Pancost, R. D. (2010). Alkenone and boron-based Pliocene pCO_2 records. *Earth and Planetary Science Letters*, *292*(1), 201–211. https://doi.org/10.1016/j.epsl.2010.01.037

Steinberger, B. (2016). Topography caused by mantle density variations: Observation-based estimates and models derived from tomography and lithosphere thickness. *Geophysical Journal International*, *205*(1), 604–621. https://doi.org/10.1093/gji/ggw040

Tackley, P. J., Stevenson, D. J., Glatzmaier, G. A., & Schubert, G. (1994). Effects of multiple phase transitions in a three-dimensional spherical model of convection in Earth's mantle. *Journal of Geophysical Research*, *99*(B8), 15877–15901. https://doi.org/10.1029/94JB00853

Taylor, W. R. (1998). An experimental test of some geothermometer and geobaro-meter formulations for upper mantle peridotites with application to the ther-mobarometry of fertile lherzolite and garnet websterite. *Neues Jahrbuch für Mineralogie - Abhandlungen*, *172*(2–3), 381–408. https://doi.org/10.1127/njma/172/1998/381

Thorkelson, D. J., Madsen, J. K., & Sluggett, C. L. (2011). Mantle flow through the Northern Cordilleran slab window revealed by volcanic geochemistry. *Geology*, *39*(3), 267–270. https://doi.org/10.1130/G31522.1

Waelbroeck, C., Labeyrie, L., Michel, E., Duplessy, J. C., McManus, J. F., Lambeck, K., et al. (2002). Sea-level and deep water temperature changes derived from benthic foraminifera isotopic records. *Quaternary Science Reviews*, *21*(1), 295–305. https://doi.org/10.1016/S0277-3791(01)00101-9

Wang, J., Hattori, K. H., Li, J., & Stern, C. R. (2008). Oxidation state of Paleozoic subcontinental lithospheric mantle below the Pali Aike volcanic field in southernmost Patagonia. *Lithos*, *105*(1), 98–110. https://doi.org/10.1016/j.lithos.2008.02.009

Wang, Y., Liu, L., & Zhou, Q. (2022). Topography and gravity reveal denser cratonic lithospheric mantle than previously thought. *Geophysical Research Letters*, *49*(1), e2021GL096844. https://doi.org/10.1029/2021GL096844

Yamauchi, H., & Takei, Y. (2016). Polycrystal anelasticity at near-solidus temperatures. *Journal of Geophysical Research: Solid Earth*, *121*(11), 7790–7820. https://doi.org/10.1002/2016JB013316

Zandt, G., & Humphreys, E. (2008). Toroidal mantle flow through the western U.S. slab window. *Geology*, *36*(4), 295–298. https://doi.org/10.1130/G24611A.1

Zheng, L., Gordon, R. G., & Kreemer, C. (2014). Absolute plate velocities from seismic anisotropy: Importance of correlated errors. *Journal of Geophysical Research: Solid Earth*, *119*(9), 7336–7352. https://doi.org/10.1002/2013JB010902

Zhong, S., Gurnis, M., & Hulbert, G. (1993). Accurate determination of surface normal stress in viscous flow from a consistent boundary flux method. *Physics of the Earth and Planetary Interiors*, *78*(1), 1–8. https://doi.org/10.1016/0031-9201(93)90078-N

References From the Supporting Information

Richards, F. D., Hoggard, M. J., Cowton, L. R., & White, N. J. (2018). Reassessing the thermal structure of oceanic lithosphere with revised global inventories of basement depths and heat flow measurements. *Journal of Geophysical Research: Solid Earth*, *123*(10), 9136–9161. https://doi.org/10.1029/2018JB015998